



A physically-based high temperature yield strength model for 9Cr steels

Title	A physically-based high temperature yield strength model for 9Cr steels
Author(s)	Barrett, Richard A.;O'Donoghue, Padraic E.;Leen, Sean B.
Publication Date	2018-05-24
Publisher	Elsevier
Repository DOI	10.1016/j.msea.2018.05.086

A physically-based high temperature yield strength model for 9Cr steels

Richard A. Barrett^{1,2}, Padraic E. O'Donoghue^{2,3}, Sean B. Leen^{1,2}

¹Mechanical Engineering, College of Engineering and Informatics, NUI Galway, Galway, H91 HX31, Ireland

²Ryan Institute for Environmental, Marine and Energy Research, NUI Galway, Galway, H91 HX31, Ireland

³Civil Engineering, College of Engineering and Informatics, NUI Galway, Galway, H91 HX31, Ireland

Corresponding Author: Richard A. Barrett

Email: richard.barrett@nuigalway.ie

Tel.: +353 (0)91 492792

Keywords: 9Cr steels; Solid solution strengthening; Laves phase; Martensitic laths; Precipitate hardening

Abstract: The strength of 9Cr steels, which is controlled by chemical composition and microstructure, evolves significantly under high temperature loading. This paper presents a temperature-independent, physically-based model for evolving yield strength, including the interdependent effects of dislocations, solutes, precipitates and grain boundaries. The key roles of solute and precipitate strengthening in 9Cr steels are successfully predicted. The measured significant beneficial effect of up to 3 wt.% tungsten on solute strengthening, and hence, yield strength are successfully predicted. The new model demonstrates that the reported strength reduction in 9Cr-3W alloys under thermal aging can be primarily attributed to Laves phase formation and associated depletion of tungsten solutes, consistent with microstructural observations.

1. Introduction

The worldwide goal of cleaner and more sustainable energy production has led to (i) highly flexible operation of conventional power plants, to supplement unpredictable renewable energy sources, and (ii) higher plant operating temperatures and pressures, to improve efficiency. The net result is an increase in thermal cycling of existing power plant with greater thermal gradients, and hence, susceptibility of critical plant components to thermo-mechanical fatigue (TMF), as well as accelerated creep, corrosion and oxidation. Thus, the range of mechanisms of microstructural degradation is expanding due to the interactions of creep, fatigue and oxidation, with the determination of continually evolving fundamental mechanical properties such as yield strength becoming much more difficult.

9Cr steels are widely considered the optimum material for heavy wall power plant components due to their relatively low coefficient of thermal expansion and cost and excellent high temperature properties. The high strength of 9Cr steels is attributed to the complex precipitate and solute-strengthened hierarchical microstructure. This hierarchical microstructure consists of prior austenite grains, packets and blocks, demarcated by high angle grain boundaries (HAGBs), as illustrated schematically in Figure 1. It has been shown that this HAGB microstructure exhibits a Hall-Petch type effect on yield strength in Fe-0.2C martensitic alloys at room temperature, which is controlled by the mean block size [1]. The martensitic transformation during heat treatment also leads to a high dislocation density (1×10^{14} to 1×10^{15} m⁻²) and the formation of a low-angle boundary (LAB) dislocation substructure (e.g. martensitic laths) within the blocks. Recovery, during tempering or service, results in coarsening of the lath microstructure leading to lath coalescence, via LAB dislocation

annihilation [2], or the formation of subgrains, where polygonisation of the microstructure leads to the formation of a coarser, more equi-axed dislocation substructure [3]. Coarsening of the LAB dislocation substructure is primarily driven by inelastic deformation at temperatures below 600 °C [4]. However, under higher temperature or longer duration tempering conditions, thermally-driven recovery of the LAB dislocation substructure can occur [5], leading to lath coarsening or formation of a coarser subgrain microstructure.

In the 'as-received' condition, precipitate strengthening is due to the presence of $M_{23}C_6$ carbides ($M = Cr, Fe, Mn, Mo, W$) at boundaries and MX carbonitrides ($M = Nb, V; X = C, N$) dispersed throughout the microstructure [6]. These particles generate an Orowan pinning mechanism to retard the motion of dislocations [4,6] and to pin boundaries. Prolonged high temperature exposure results in a coarsening of these precipitates and the formation of secondary phase particles, such as Laves phase (Fe_2Mo, Fe_2W) and Z-phase (complex $(Cr,Fe)(Nb,V)N$ nitrides) particles [7]. The Laves phase particles form at the expense of Mo and W solutes, with the Z-phase particles consuming the MX carbonitrides. Numerous authors have measured the increase in mean precipitate diameter with creep and thermal aging [4,6,8].

Solid solution strengthening is another key source of strength in 9Cr alloys and is dominated by the presence of Mo and W substitutional solute atoms within the microstructure. However, other elements such as Cr, Mn and Si are known to provide significant strengthening in Fe-alloys [9] and hence, potentially play a significant role in strengthening of 9Cr steels. The interstitial atoms (B, C and N) predominantly form carbides ($M_{23}C_6$ particles) and carbonitrides (MX particles) [10] and the level of strengthening via interstitials in 'as-received' 9Cr steels is not as significant as the substitutional solute atoms. It has recently been shown that the addition of up to 3 wt.% W in 9Cr steels (e.g. MarBN alloys) contributes up to 36% improvement of yield strength compared to modified P91 steel [11,12]. This significant increase in yield strength is attributed to the increased solute and precipitate hardening. Increased W content can also retard carbide coarsening [8]. However, beyond 3 wt.% W, the δ -ferrite volume fraction exceeds acceptable levels for 9Cr steels, resulting in a dual phase material with reduced precipitate and LAB strengthening [8]. The inclusion of small amounts of boron (approximately 140 ppm [10]) can also reduce $M_{23}C_6$ carbide spacing via formation of a finer distribution of more thermally stable $M_{23}(CB)_6$ carbides and, hence, maintain a hierarchical microstructure following welding [13]. This is crucial for the high creep strength of weldments. It is also widely known that excessive Al in composition can result in AlN particle formation at the expense of thermodynamically stable VN carbonitrides [14], a critical strengthening mechanism for 9Cr steels. Thus, chemical composition represents a key input in the determination of the performance and mechanical properties, such as yield strength, of 9Cr steels. Similarly, heat treatment can have a significant effect on yield strength. Excessive normalisation or tempering can lead to coarsened precipitate microstructures and precipitation of additional inter-metallic phases [7], affecting grain size and dislocation density [5] and leading to significant variations in LAB dimension [5].

Although a relatively homogeneous microstructure exists in parent material 9Cr steels, manufacturing processes such as welding give rise to complex microstructural evolution processes, leading to regions of martensite, α -ferrite, retained austenite and δ -ferrite, as well as

significant deviations in precipitate and solute microstructures. In such heterogeneous and irregular microstructures, determination of an accurate yield strength is difficult and further complicated by a convoluted microstructural evolution during service. Thus, the complexity of microstructural evolution in 9Cr steel weldments during creep-fatigue-oxidation deformation requires the definition of yield strength from a physical basis.

The modelling of specific mechanisms contributing to yield strength in metallic alloys is well established for a range of effects, such as the Peierls-Nabarro stress [15,16], Hall-Petch effect [17,18], solid solution strengthening [9,19,20] and precipitate hardening [21]. These strengthening mechanisms have been investigated for a range of alloys. For example, Morito *et al.* [1] measured the effect of grain size on yield strength in low carbon martensitic alloys. Shibata and co-workers [22] extended this experimental work to explicitly account for high- and low-angle boundary contributions to yield strength via analysis of micro-bend tests. The effect of phase was incorporated within a physically-based model for yield strength using a rule of mixtures approach for Co-Ni alloys in the work of Wang *et al.* [23]. This work also accounts for the key role of precipitates, solutes and the Hall-Petch effect. In terms of modelling the yield strength of 9Cr steels from a physical basis, the model of Li [24] has been successfully applied to room temperature behaviour of 'as received' P91. Yan *et al.* [25] have accounted for the evolution of precipitates, laths and dislocations as a function of aging time on yield strength in a 9Cr-3W-3Co alloy and Wang and co-workers [26] recently developed a multi-scale model incorporating the effect of irradiation, MX precipitates and grain size in reduced-activation ferritic-martensitic steels. Although a number of authors have accounted for a loss of dislocation substructure due to LAB dislocation annihilation as a function of cycles under low-cycle fatigue [2,27], no temperature-independent multi-mechanism framework currently exists for predicting the effect of LAB strengthening and solute atoms from a physical basis in 9Cr steels.

The approach of the current paper is to develop a chemical composition and microstructure-driven framework for predicting yield strength in 9Cr steels. This model will account for key strengthening and degradation mechanisms including (i) the inhomogeneous distribution of precipitates in the microstructure and loss of precipitate strengthening, (ii) evolution of solid solution strengthening and (iii) the role of material phase (martensite, retained austenite or δ -ferrite). The proposed model is validated against Ni-alloys for solid solution strengthening and low carbon martensitic alloys to quantify the contribution of grain boundaries (GBs) and C interstitials to yield strength. The model is then applied to 9Cr steels across a range of different temperatures, compositions and loading histories to predict yield strength in such alloys and to estimate the contribution of the individual strengthening mechanisms.

2. Methodology

As discussed by Kocks *et al.* [28], the yield stress of a metallic alloy consists of two distinct contributions: (i) strength due to the presence of dislocations in the material, τ_A , and (ii) the contribution of obstacles such as particles and boundaries, τ_B , to yield strength. The work of Kocks also suggested that a microstructure-driven root mean square approach results in a more accurate prediction of yield stress compared to a linear summation of the dislocation and

obstacle strengthening terms; this concept has also been verified for martensitic alloys at room temperature [24]. Thus, in the present work, the yield stress is defined as:

$$\sigma_y = M(\tau_A^2 + \tau_B^2)^{1/2} \quad (1)$$

where M is the Taylor factor. The contribution of dislocations is defined using a Taylor hardening expression:

$$\tau_A = \alpha_1 \mu b \sqrt{\rho} \quad (2)$$

where α_1 is a material constant between 0.2 and 0.5, μ is temperature-dependent shear modulus, b is magnitude of Burgers vector and ρ is dislocation density. The contribution of particles and GBs to yield strength is defined as the sum of the individual obstacle strengthening terms:

$$\tau_B = \tau_{PN} + \tau_{bd} + \tau_{ss} + \tau_{ph} + \tau_{in} \quad (3)$$

where τ_{PN} is the Peierls-Nabarro stress, τ_{bd} is the contribution of GBs to strength, τ_{ss} is the strength provided by solute atoms, τ_{ph} is the contribution of precipitates to yield strength and τ_{PN} is strengthening due to interstitial atoms. It is assumed here that the materials have not undergone work hardening and hence, this term is neglected. The following sections detail the contributions of the Peierls-Nabarro stress, GBs, solutes and precipitates to the yield stress.

2.1. Peierls-Nabarro Stress

The Peierls-Nabarro stress is the shear stress required to move a dislocation in the absence of other strengthening mechanisms (i.e. intrinsic strength of a metal). Peierls [15] defined this stress to be a function of the width of a dislocation. However, as discussed by Foreman *et al.* [29], the model of Peierls under-predicted the width of a dislocation and hence, compared with real crystals, the Peierls model over-predicted the intrinsic strength of a material. Thus, the model of Nabarro [16] is used in the present work:

$$\tau_{PN} = \frac{2\mu}{1-\nu} \exp\left(\frac{-2\pi}{1-\nu}\right) \quad (4)$$

where ν is Poisson's ratio.

2.2. Contribution of grain boundaries to yield strength

HAGBs cause pinning of dislocations and hence, retardation of dislocations and resistance to inelastic deformation. This HAGB strengthening is simulated using the well-known Hall-Petch equation. Based on the measured data of Sakui *et al.* [30,31] for pure Fe, an exponential dependence of the Hall-Petch constant, k_{HP} , on temperature is observed (see Figure 2). Thus, the HAGB contribution to strength is:

$$\tau_{HP} = \frac{k_{HP}(T)}{d_g^{n_{HP}}} = k_{HP,0} \exp\left(\frac{-T}{T^*}\right) \frac{1}{d_g^{n_{HP}}} \quad (5)$$

where $k_{HP,0}$ is the Hall-Petch constant at 0 K, T^* is a constant, d_g is grain size and n_{HP} is the Hall-Petch exponent with a value of approximately $\frac{1}{2}$. In a material with a hierarchical microstructure, d_g is assumed to be the minimum HAGB dimension (the mean block width, d_b). In such materials, the contribution of GBs to yield strength must also account for the strengthening due to the LAB dislocation substructure, τ_{LAB} . Thus, the overall increase in yield stress due to GBs is:

$$\tau_{bd} = \tau_{HP} + \tau_{LAB} \quad (6)$$

As discussed by Maruyama *et al.* [32], τ_{LAB} is inversely proportional to the dimension of the LAB, \bar{m} . Thus, the contribution to yield strength from the LAB dislocation substructure is:

$$\tau_{LAB} = \frac{\alpha_2 \mu b}{\bar{m}} \quad (7)$$

where α_2 is a material parameter with a value between 2 and 3. The LAB dislocation substructure can be in either subgrain (equi-axed LABs) or martensitic lath (elongated subgrain LABs) form, as illustrated schematically in Figure 3. The maximum dimension of the martensitic lath, l , is assumed to be $\frac{1}{3}$ of the packet width, d_p . Thus, an equivalent LAB dimension is defined using the mean slip length model of Naylor [33]:

$$\bar{m} = \frac{2}{\pi} \left[w \ln \left(\tan(\arccos(w/l)) + \frac{l}{w} \right) + l \frac{\pi}{2} - l \arccos \left(\frac{w}{l} \right) \right] \quad (8)$$

where w is the LAB width. The right-hand side of Equation (8) reduces to w for an equi-axed subgrain microstructure (i.e. for $l = w$).

2.3. Solid solution hardening

Solute atoms generate a local stress field in the matrix material and hence, increase the shear stress required to move dislocations in the vicinity of solute atoms. The local stress field is produced via interactions with solvent atoms, including (i) atomic size mismatch, (ii) shear modulus mismatch, (iii) electrical interaction and (iv) chemical interactions. In metallic alloys, the contribution of solute atoms to yield strength is dominated by atomic size and shear modulus mismatch. Solute atoms can exist in either binary or multi-component solid solution form and typically follow the Hume-Rothery rules (i.e. the optimum solute strengthening is provided by solute atoms typically with an atomic size mismatch of less than 15%). The contribution of m multi-component substitutional solutes to the overall yield strength is [35]:

$$\tau_{ss}^p = \sum_{i=1}^m \tau_{ss,i}^p \quad (9)$$

where the constant p is the inverse of the concentration exponent and $\tau_{ss,i}$ is the increase in shear stress due to solute i . The concentration exponent, p , varies for dilute and concentrated solutions (e.g. $\frac{3}{2}$ for concentrated solutions and 2 for dilute solutions). To evaluate the shear stress contribution due to solute atoms, the Labusch solid solution strengthening model [20] is used:

$$\tau_{ss,i} = \frac{A}{b} \left(\frac{F_{m,i}^4 \varpi}{\Gamma} \right)^{1/3} \left(\frac{c_i}{l_{0,i}^2} \right)^{2/3} \quad (10)$$

where A is a constant with a value of approximately unity, $F_{m,i}$ is maximum solute atom-dislocation interaction force, ϖ is the range of interaction, Γ is dislocation line tension, c_i is solute concentration and $l_{0,i}$ is the mean spacing of solute i . In the present work, it is assumed that a dislocation needs to extend approximately 2 to 3 lattice spacings before yielding occurs [36] and hence ϖ is in the range of $2d$ to $3d$, where d is the lattice spacing. The dislocation line tension is approximately $\mu b^2/2$ and the mean spacing of solutes, estimated using the geometry presented in Figure 4, is:

$$l_{0,i} = \left(\frac{2}{c_i^{1/3}} - 3 \right) b_{\text{mtx}} + 2 \left(\frac{b_{\text{mtx}} + b_{\text{sol},i}}{2} \right) \quad (11)$$

where b_{mtx} is magnitude of Burgers vector for matrix material and $b_{\text{sol},i}$ is magnitude of Burgers vector for solute i . The maximum solute atom-dislocation interaction force, $F_{m,i}$, is [37]:

$$F_{m,i} = \frac{\mu b^2}{\varphi} \varepsilon_{L,i} \quad (12)$$

where φ is a numerical constant and ε_L is the misfit parameter, defined as:

$$\varepsilon_L = \left[\left(\frac{\varepsilon_\mu}{1 + 0.5|\varepsilon_\mu|} \right)^2 + (\alpha \varepsilon_b)^2 \right]^{2/3} \quad (13)$$

where ε_b is the lattice misfit parameter ($\partial b/\partial c \times 1/b$), ε_μ is the shear modulus misfit parameter ($\partial \mu/\partial c \times 1/\mu$) and α is a constant in the range of 3 to 15. The specific material properties μ , ν and b are determined using a rule of mixtures approach. Table 1 contains the physical parameters [38] used to determine the solid solution strengthening misfit parameters. Vegard's law is used to define the evolution of lattice parameters with solute concentration. The phase-specific material parameters are defined in Table 2.

The presence of C and N atoms at interstitial crystal lattice sites is accounted for using the simplified assumption that the increase in strength is proportional to the composition in wt.% to the power of 1/2 [40]:

$$\tau_{in} = \frac{1}{M} \left\{ k_C [\text{C(wt.\%)}]^{1/2} + k_N [\text{N(wt.\%)}]^{1/2} \right\} \quad (14)$$

where k_C and k_N are the hardening constants for C and N interstitials, respectively.

2.4. Precipitate Strengthening

Assuming that the contribution of chemical precipitate strengthening is negligible and that the mean radii of particles exceeds the critical radius for transition from shearing to dislocation

bowing, the method of strengthening via precipitates in the microstructure is due to pinning of dislocations (Orowan strengthening). Hence, the contribution to yield strength by precipitates is defined using the Ashby-Orowan equation [21]:

$$\tau_{\text{ph}} = 0.045 \frac{\mu b}{\lambda} \ln \frac{r}{b} \quad (15)$$

where λ is mean inter-particle spacing and r is particle radius.

In 9Cr steels, secondary phase particles, which form during the heat treatment process and evolve during high temperature- and strain-dependent loading, are a key strengthening mechanism. In the initial microstructure, it is assumed that two primary types of precipitates are formed, (i) $M_{23}C_6$ carbides dispersed along boundaries and (ii) MX carbonitrides distributed uniformly throughout the microstructure. Hence, to account for the heterogeneous distribution of carbides within the microstructure of 9Cr steels, a rule of mixtures approach is used to define the contribution of precipitates to the yield strength:

$$\tau_{\text{ph}} = (1 - f_w - f_g) \tau_{\text{ph,INT}} + (f_w + f_g) \tau_{\text{ph,BND}} \quad (16)$$

where $\tau_{\text{ph,INT}}$ is the proportion of the precipitate yield strength in the martensitic lath interiors, $\tau_{\text{ph,BND}}$ is the precipitate yield strength at the GBs and f_g and f_w are the volume fractions of the high-angle and low-angle boundaries, respectively. The definitions of f_w and f_g are described in detail elsewhere [27]. Application of Equation (16) in conjunction with Equation (15) for 9Cr steels requires definition of (i) mean particle spacing, λ , and (ii) mean particle radius, r , for each region within a multi-precipitate type system. This is detailed in Appendix A.

3. Results and Discussion

3.1. Simulating solid solution strengthening in Ni-based alloys

To validate the performance of the solid solution strengthening model, predictions of yield strength in pure nickel and nickel binary alloys are performed and compared with the experimental data of Mishima *et al.* [41]. The tests were conducted at 77 K and the Ni-based alloys are considered to be precipitate- and interstitial-free fcc microstructures. Hence, martensitic lath strengthening, precipitate hardening and interstitial solid solution strengthening are not considered for the Ni-alloy predictions.

The dislocation density of pure Ni is in the range of 2.88×10^{12} to $1.0 \times 10^{13} \text{ m}^{-2}$ [42,43], with the grain size of the Ni-alloys within the 100 to 300 μm range [41]. Mean values of $6.44 \times 10^{12} \text{ m}^{-2}$ and 200 μm are assumed for dislocation density and grain size, respectively. Furthermore, Fe is considered to be in the γ -phase, with the magnitude of Burgers vector as presented in Figure 5. The Hall-Petch constant is identified from the slope of yield strength versus the inverse of grain size as presented in Figure 6, resulting in a mean value of $0.233 \text{ MPa.m}^{1/2}$.

Using Equations (2), (4) and (5), the contributions of the dislocations, the Peierls-Nabarro stress and GBs to yield strength are estimated to be $24 \pm 7 \text{ MPa}$, 24 MPa and $5.3 \pm 1.5 \text{ MPa}$, respectively, for pure Ni. Hence, the total yield stress is estimated at $116 \pm 17 \text{ MPa}$, which is in close agreement with the mean measured value of 104 MPa [41]. The predicted tolerance of

± 17 MPa for pure Ni yield strength is achieved via consideration of the typical ranges of measured dislocation density and grain size in pure Ni [41,42,43].

Figure 7 presents a comparison of the predicted and experimentally observed [41] variation in yield strength as a function of solute concentration. In general, close correlation is achieved with the measured data for the majority of solute elements, illustrating the ability of the proposed model to predict the contribution of solid solution strengthening in fcc Ni-based alloys. In particular, the incorporation of the new solute spacing function of Equation (11) enables the general trend and shape of the yield strength as a function of concentration to be captured. The slight over-prediction of strength for solute concentrations in excess of 8 at.% in the Ni-Ti and Ni-W alloys may be related to the potential formation of Ni_3Ti and Ni_4W particles in such steels and hence, a non-uniform and reduced distribution of solute atoms in the fcc Ni matrix. The model-predicted error bars in Figure 7 represent the reported variation of (i) dislocation density, (ii) k_{HP} and (iii) grain size for the range of Ni alloys [41]. It should also be noted that the small variations in chemical composition are not accounted for in the choice of k_{HP} . Figure 7d presents a direct comparison of the experimentally-measured yield strength with the model-predicted values. The maximum error is 20%, with a mean error of 9% and standard deviation of 6%.

Although a wide range of models exist for solid solution strengthening [9,19,37], the statistical Nabarro-Labusch model of Equation (10), including a modification to incorporate the definition of mean spacing of solutes presented in Equation (11), is thus found to predict the contribution of solid solution strengthening to a high degree of accuracy. Leyson and Curtin [48] have shown that the increase in solute shear strength is proportional to $c^{2/3}$ when the concentration is relatively high, i.e. in excess of 100 to 200 ppm (or 0.1 to 0.2 at.%), which is the case for the substitutional elements of the Ni alloys presented here. This is also the case for solid solution strengthening in 9Cr steels, as discussed below.

3.2. Predicting the contribution of high and low-angle boundaries to yield strength

The effect of hierarchical microstructure on the yield strength of martensitic alloys is determined here via consideration of measured values in low carbon alloys at room temperature. The purpose of this study is to (i) calibrate the bcc model parameters (α , φ and α_2) for application to 9Cr steels, (ii) determine the constant k_C and (iii) investigate the contribution of the individual strengthening mechanisms to yield strength in martensitic alloys. Specifically, the model will be applied to:

1. Quantify LAB and HAGB contributions to yield strength in an Fe-23Ni martensitic alloy via comparison with (i) a coarse-grained, low dislocation density ferritic alloy (Fe-1.5Mn(Low ρ)) without a hierarchical microstructure, (ii) a high dislocation density ferritic alloy (Fe-1.5Mn(High ρ)) without consideration of the HAGBs [22] and (iii) micro-bend test results on Fe-23Ni martensitic alloys with and without a block boundary [22].
2. Simulate C interstitial solute strengthening in Fe-C alloys via comparison with the experimental data of Krauss [40].

- Predict the effect of HAGB dimension on yield strength in Fe-0.2C and Fe-0.2C-2Mn alloys as measured by Morito *et al.* [1], and to validate the model-predicted contribution of Mn solute atoms.

The chemical compositions of the various alloys are presented in Table 3. The microstructures of the Fe-23Ni and Fe-C alloys are lath martensite [49,50]. The lath width for Fe-23Ni is 0.23 μm [22]. The lath width of the Fe-0.2C alloy is estimated at 0.26 μm [51] and 0.23 μm for the Fe-0.2C-2Mn alloy [1]. The dislocation density for Fe-1.5Mn(High ρ) ferritic and the Fe-23Ni and Fe-C martensitic alloys are taken from measured results [22, 49], with the dislocation density of Fe-1.5Mn(Low ρ) ferrite approximated as $1.0 \times 10^{13} \text{ m}^{-2}$ [7]. For the Fe-23Ni alloy, d_b is 2.46 μm and k_{HP} is 0.21 $\text{MPa}\cdot\text{m}^{1/2}$ [22]. The constant k_{HP} for the Fe-1.5Mn and Fe-C alloys is set at 0.18 $\text{MPa}\cdot\text{m}^{1/2}$, the value for pure Fe at room temperature [30]. The solute strengthening constants, α and ϕ , are identified using a best fit with Fe-23Ni experimental data, with the model parameters for Fe alloys presented in Table 2.

Figure 8a presents a comparison of the predicted and experimentally observed yield strengths in (i) coarse-grained ferritic Fe-1.5Mn(Low ρ) alloy (no martensitic laths), (ii) Fe-1.5Mn(High ρ) ferrite without GBs and martensitic laths, (iii) Fe-23Ni martensitic alloy without a HAGB and (iii) Fe-23Ni martensitic alloy with a HAGB (Fe-23Ni(HAGB)). In all cases, an accurate correlation with the experimentally observed yield strength values is achieved, with the error bars reflecting the measured variation in dislocation density as discussed in detail by Morito *et al.* [49]. Figure 8b presents a breakdown of the shear strength contributions to yield strength. Compared with the Fe-1.5Mn(Low ρ) coarse-grained ferritic alloy, an increase in yield strength is predicted for the Fe-1.5Mn(High ρ) due to the significant increase in dislocation density. A significant increase in yield strength is predicted for the martensitic Fe-23Ni alloys compared with the Fe-1.5Mn ferritic alloys, due predominantly to the hierarchical microstructure (combination of LAB strengthening and associated high dislocation density) and solid solution strengthening provided by the Ni solute atoms. A comparison of the model predicted yield strength with and without the HAGB microstructure highlights that the contribution of the HAGB strengthening is approximately equivalent to that of the martensitic lath microstructure for the specific block size considered here. This result illustrates the importance of the different strengthening mechanisms present in martensitic alloys and the requirement to account for these within a physically-based modelling methodology for martensitic alloys.

Figure 9a presents the measured effect of carbon content on microstructural properties in Fe-C steels. The dislocation density increases with increasing carbon content [49] due to the decreasing block and lath width, as measured in [52]. Below a carbon content of approximately 0.12 wt.%, the microstructure is predominantly ferritic [40]. Figure 9b presents application of the proposed model to Fe-C alloys as a function of carbon content. Using a least squares approach, an optimised value of $551 \text{ MPa}\cdot\text{wt}\%^{-1/2}$ is identified for the carbon interstitial strengthening constant, k_C . The proposed modelling methodology results in close correlation with measured data for both ferritic and martensitic Fe-C alloys. The identified value of k_C is substantially lower than the value of $1310 \text{ MPa}\cdot\text{wt}\%^{-1/2}$ identified by Krauss [40]. This difference is due to the incorporation of the carbon-dependent microstructure of Fe-C alloys

(see Figure 9a) within the yield strength model, further highlighting the importance of dislocation strengthening and GB hardening in modelling hierarchical microstructures.

The model is applied to Fe-0.2C and Fe-0.2C-Mn alloys across a range of block sizes in Figure 10. It has been shown that dislocation density and lath width are largely independent of block size in Fe-0.2C and Fe-0.2C-Mn alloys [1]. Furthermore, the substitutional and interstitial solid solution strengthening effect remains constant with decreasing grain size as it is assumed that precipitation of secondary phase particles does not occur. The model predicts excellent correlation with experimental data across all block widths. At large block sizes, where the effective strengthening of the blocks is minimal, the model predicts yield stresses of 520 MPa and 782 MPa for Fe-0.2C and Fe-0.2-2Mn, respectively. These values are within 5% of a linear extrapolation of the measured data of Morito *et al.* [1] to higher block widths, where the Hall-Petch contribution is negligible. The results of Figure 10a also illustrate the ability of the model to predict the contribution of the Mn solute atoms to yield strength. A breakdown of the obstacle shear stress contributions to yield strength is presented in Figure 10b. Based on the measured microstructures, the difference in predicted yield strength between the two alloys is due to (i) 2 wt.% Mn solute atoms, (ii) dislocation density and (iii) LAB strengthening. The contributions to solid solution strengthening obtained using the modified Labusch model presented in Equation (10) are in reasonably close agreement with those obtained using the Lacy and Gensamer [9] constants, further validating the proposed solid solution strengthening model. The estimated Peierls-Nabarro stress in the range of 30 to 33 MPa is consistent with measured values of between 13 and 55 MPa [53].

3.3. Physically-based yield strength modelling of 9Cr steels

The proposed physically-based yield strength model is applied to 9Cr steels across a range of chemical compositions and temperatures. Uniaxial tensile tests were performed on two 9Cr alloys, namely P91 steel and MarBN (a new 9Cr steel with up to 3 wt.% W and Co with controlled levels of B and N), at temperatures in the range of 293 K to 923 K. The typical chemical compositions of both alloys are presented in Table 4. The MarBN alloy presented here is in cast form. The temperature-dependent tensile response of the P91 alloy is presented in Figure 11. Figure 12 presents a comparison of the stress-strain responses of the two 9Cr alloys, with a significant increase in strength observed for MarBN when compared with P91. For 9Cr steels, it is clear that the material stress-strain response is highly non-linear for a 0.2% proof strength. It is evident from Figures 11 and 12 that a 0.2% offset definition of yield strength is not appropriate here (due to significant non-linearity). Hence, we define yield strength in terms of 0.02% offset in this paper.

The measured microstructures of rolled P91 and cast MarBN are presented in Figure 13. MarBN has a coarser hierarchical microstructure compared to the rolled P91 steel as a result of the heat treatment process. The mean block sizes of P91 and MarBN alloys are estimated at 6.7 μm [54] and 14 μm , respectively. Both alloys exhibit a martensitic lath dislocation substructure. For example, the transmission electron microscopy (TEM) image presented in Figure 14 shows this for MarBN. Thus, the 36% increase in yield strength for MarBN (see Figure 12) cannot be attributed to a Hall-Petch type mechanism. The martensitic lath width is

0.7 μm for P91 [2] and 0.325 μm for MarBN [25]. The dislocation density is $1.6 \times 10^{14} \text{ m}^{-2}$ for P91 [2] and $2.65 \times 10^{14} \text{ m}^{-2}$ for MarBN [55]. The composition of atoms in solution is presented in Figure 15 for P91 (estimated using the nominal chemical composition presented in Table 4 minus the composition of precipitates) and MarBN (determined using ThermoCalc simulations [56]), respectively. The corresponding individual element contributions to τ_{ss} are also shown in Figure 15 for P91 and MarBN at temperatures of 273 K and 873 K. The solute strengthening is dominated by Mo and W for P91 and MarBN, respectively, with a significantly increased solute contribution predicted for MarBN ($\tau_{\text{ss}} = 29.9 \text{ MPa}$ at 273 K) compared with P91 ($\tau_{\text{ss}} = 19.5 \text{ MPa}$ at 273 K). It is assumed that the levels of dissolved carbon and nitrogen are quite small (approximately $6 \times 10^{-6} \text{ wt.}\%$ and $1 \times 10^{-6} \text{ wt.}\%$, respectively [24]) and thus contribute less than 2 MPa to the yield strength at room temperature. Hence, for 9Cr steels containing carbide and carbonitride precipitates, the effect of C and N interstitials is assumed to be minimal for 'as received' 9Cr steels. The volume fraction and radii of the M_{23}C_6 and MX (VN and NbC) precipitates are taken from published data for similar materials [7,8,12,32,57] and presented in Table 5. The temperature-dependencies of shear modulus, determined from the experimental data of Figure 12, and Poisson's ratio (determined based on bulk and shear modulus data [58]) are illustrated in Figure 16.

Application of the proposed model here to 9Cr steels is presented in Figure 17 across a range of temperatures. Given that MarBN has a significantly coarser HAGB microstructure, one might superficially expect it to have a lower strength than P91. However, it has an increased yield strength which is attributed to (i) higher solid solution strengthening, as highlighted in Figure 15, (ii) slightly higher dislocation strengthening and (iii) higher shear modulus with up to 3 wt.% W in the composition (e.g. see Table 1). The higher solid solution strengthening in MarBN with increasing temperature is predominantly due to the W solutes (Figure 15). Figure 15 also shows a large solid solution strengthening contribution from Mn, Ni and Si solute atoms in 9Cr steels, due to the high lattice mismatch between Fe matrix and Mn and Ni solute atoms and a significant modulus mismatch between Si and Fe atoms. The inclusion of 3 wt.% Co within the MarBN microstructure is determined to cause only a small increase in yield strength as the shear modulus and lattice parameter of Co are similar to those of Fe atoms.

Figure 18 presents a breakdown of the mechanistic contributions to strength across a range of temperatures for MarBN. A key finding is that obstacle strengthening in 9Cr steels is contributed to almost equally by the different key mechanisms represented here. This is even more important for materials under typical service conditions with microstructure evolution. For example, loss of dislocation substructure and carbide coarsening occur under creep loading, and depletion of solute atoms occurs under thermal aging, leading to significant effects on yield strength.

3.4. The role of W on yield strength

The proposed model is applied to predict the role of W on the yield strength of 9Cr steels, both at room temperature and at 873 K, as measured by Park *et al.* [12]. Park *et al.* [12] present the compositions; the heat treatment procedure consists of normalisation at 1323 K followed by tempering for 1 hr at 1023 K.

The precipitate microstructure is a function of the W content; increasing W content reduces precipitate diameter and retards particle coarsening at high temperatures [59], hence, retaining a fine precipitate microstructure during tempering. Using the data of Park *et al.* [12], an effective particle radius, r_{eff} , was determined for each precipitate type based on the measured particle area, A , i.e. $r_{\text{eff}} = \sqrt{A/\pi}$. The volume fractions of the precipitates are determined from the phase diagrams generated by Srinivas Prasad *et al.* [7], in conjunction with MX carbonitride compositions for 9Cr steels [60,61]. The volume fractions of NbC and VN carbonitrides are assumed to be dependent on W content [60]; increasing W increases the NbC and VN volume fractions. Although there is a decrease in the volume fraction of Mo_{23}C_6 carbides with increasing W content, the increase in M_{23}C_6 carbide volume fraction is expected due to the formation of additional W_{23}C_6 carbides in W-containing steels. The simulations of Srinivas Prasad *et al.* [7] were carried out on conventional P91 and P92 steels with similar composition to the 9Cr-1Mo (0W) and 9Cr-0.5Mo-1.8W materials of Park *et al.* [12]. The volume fraction of the 1.2W and 2.7W alloy precipitates were estimated using linear interpolation. The concentration of atoms in solid solution is taken as the nominal concentration minus the concentration of each element in precipitate form. For M_{23}C_6 carbides, the concentration of Cr, Fe, Mo and W in precipitate form is measured in the work of Park *et al.* [12], with similar results observed elsewhere for 9Cr steels [6,61,62]. The resulting estimated chemical composition in solid solution form is presented in Figure 19.

The initial dislocation density in 9Cr alloys is in the range of $1.6 \times 10^{14} \text{ m}^{-2}$ to $2.65 \times 10^{14} \text{ m}^{-2}$ [2,63]. The martensitic lath width for the W-alloys is in the range of 0.3 to 0.5 μm [64,65], with lath width decreasing for increasing W. It is assumed here that the finer distribution of carbides with increasing W provides improved pinning of LABs, resulting in (i) a finer LAB dislocation substructure and (ii) an increased dislocation density due to the increased concentration of LABs.

As W content increases, δ -ferrite can form at increased normalisation temperatures. Park *et al.* [12] measured a δ -ferrite content of approximately 8% in the 2.7W alloy. δ -ferrite is effectively a carbide free region void of a martensitic microstructure and of reduced dislocation density [8]. Hence, a rule of mixtures model is used here to define the effective yield strength of the dual phase (δ -ferrite and martensite) material:

$$\sigma_y = (1 - f_{\delta\text{-Fe}}) \sigma_{y,\alpha} + f_{\delta\text{-Fe}} \sigma_{y,\delta\text{-Fe}} \quad (17)$$

where $f_{\delta\text{-Fe}}$ is the volume fraction of δ -ferrite and $\sigma_{y,\alpha}$ and $\sigma_{y,\delta\text{-Fe}}$ are the yield strengths of martensitic and δ -ferrite forms of the alloy, respectively. The dislocation density of the δ -ferrite region is approximated at $1.0 \times 10^{13} \text{ m}^{-2}$ [7] and the concentration of solute atoms is taken as the chemical composition due to the assumption of a precipitate free zone. The complete set of microstructural parameters used for the 9Cr steels with varying W content is presented in Table 6.

Figure 20 shows the predicted increase in yield strength with increasing W content at temperatures of 293 K and 873 K. Close correlation is achieved when compared with measured data [12]. Figure 20 also includes the yield strength prediction for the 2.7W alloy with 8% δ -

ferrite. This is predicted to cause less than 5% difference in yield strength compared to the prediction without including the effect of δ -ferrite. However, the work of Park *et al.* [12] illustrates the important role of δ -ferrite on fatigue life in 9Cr steels, with the HAGB interface between δ -ferrite and tempered martensite acting as a preferential site for fatigue crack initiation. Furthermore, the development of a model with the capability to predict the reduction in yield strength associated with δ -ferrite formation in tempered martensite is critical for simulating the behaviour of (i) 9Cr welded connections, and (ii) 12-15Cr alloys, where increased volume fractions of δ -ferrite (up to 60%) can form [8] and significantly reduce the strength of the material.

Figure 21 shows the resulting calculated contributions of the various strengthening mechanisms for the increasing fractions of W at 873 K (Figure 20). The main factors contributing to the increase are (i) LAB dislocation substructure and (ii) increased solid solution strengthening of the W solute atoms. Although Mo and W solute atoms have similar lattice misfit properties and the Mo equivalent (Mo_{eq}) value is approximately constant in all four alloys, it is predicted that the increase in the concentration of individual W solutes, coupled with the increased modulus misfit, causes a significant increase in yield strength of the material.

3.5. The effect of thermal aging and prior creep deformation on yield strength

The effect of secondary phase particle formation, such as Laves phase particles, on the long-term performance of 9Cr steels has been previously established [66]. The formation of these particles, which can occur during thermal operation of power plant components, can potentially increase plastic deformation via a reduction in yield strength and, hence, reduce resistance to low cycle fatigue deformation under high temperature flexible operation. Coupled with this evolution of the microstructure is carbide coarsening, dislocation density evolution and coarsening of the martensitic lath dislocation substructure.

The decrease in yield strength due to thermal aging in a 9Cr-3W-3Co (G115 steel) alloy has been measured at 923 K by Yan *et al.* [25], for the chemical composition presented in Table 4. This reduction of strength occurs concomitant with a significant evolution of the microstructure, including; (i) a decrease in dislocation density, (ii) martensitic lath widening, (iii) $M_{23}C_6$ carbide coarsening and (iv) the formation and growth of Fe_2W Laves phase particles, as characterised in detail by Yan *et al.* [25] (with Fe_2W evolution described in Ma *et al.* [57]) and presented in Table 7. It is assumed that no coarsening of the thermally-stable MX carbonitrides occurs and hence, that Z-phase particles do not form during this short test time.

Figure 22 presents predicted effect of aging time on yield strength, including and excluding Laves phase (Fe_2W) formation. It is clear that inclusion of Laves phase is critical for accurate prediction. This demonstrates the key role of W solute atoms and Fe_2W precipitation on yield stress. A small increase in precipitate strengthening is predicted due to the formation of Fe_2W particles. However, Fe_2W particles rapidly coarsen and, more importantly, deplete the matrix microstructure of W solute atoms [57]. This reduction of W solute atoms is the largest single contribution to the decrease in yield stress for short-term thermal aging.

The decrease in yield strength due to thermal aging (Figure 22) is initially rapid, but then levels out. This is partly attributed to the Laves phase volume fraction quickly reaching equilibrium

in 9Cr-3W alloys and the mean Laves phase radius achieving a saturated value. Under such conditions, the consumption of W solute atoms reduces significantly and hence, a more gradual decrease in yield stress occurs. The time taken to reach equilibrium decreases with increasing W (or Mo) content [7]. Saturation of dislocation density evolution and martensitic lath widening also contributes to the decrease in yield stress evolution rate, but not to the same extent as the depletion of W solutes.

The role of prior creep deformation is evaluated here via application of the above yield stress modelling methodology to creep-exposed (i) P91 steel in Figure 23 and (ii) cobalt-modified P92 alloy (9Cr-1.8W-3Co) in Figure 24. The chemical composition and evolution of the microstructure of the two materials is given elsewhere [4,6,67].

In Figure 23, the predicted yield strength evolution is shown following more than 100,000 hrs creep deformation at 873 K. Using the measured 'as-received' and post-creep test microstructural data of Panait and co-workers [4,6], the model predicts a 31% decrease in yield strength of P91 steel following 100,000 hrs creep testing. The measured reduction in hardness [68] of a P91 component following 9 years of service at 873 K is 36%, also shown in Figure 23. Under the assumption that yield strength is directly proportional to hardness, this result demonstrates the capability of the model to estimate the reduction in hardness of 9Cr steels under service loading conditions.

Figure 24 shows the predicted evolution of yield strength as a function of creep time. The initial predicted yield stress is in the range of 213 MPa to 220 MPa, consistent with experimental measurements for 9Cr-1.8W [69]. For the short times considered here, the significant predicted reduction in yield strength is dominated by creep strain. The evolution of the dislocation substructure contributes the largest decrease in yield strength, with dislocation density and coarsening of laths accounting for 55% and 25% of the reduction in shear stress contributions, respectively. The applied stress of 140 MPa is high relative to typical plant conditions and hence, over the lifetime of a plant component, thermal stability of the precipitate and solute microstructure remains a key requirement for plant materials and life prediction of components. The decreased W content of the cobalt-modified P92 alloy also increases resistance to Laves phase formation, compared with 9Cr-3W-3Co alloys, and reduces the equilibrium volume fraction of such particles [7]. Thus, 1.8W alloys are less susceptible to the initial rapid decrease in yield strength associated with Laves phase formation in 3W alloys as the change in concentration of W solute atoms is less severe.

4. Conclusions

The key conclusions are as follows:

- A new yield strength model which captures the interdependencies of different strengthening mechanisms in 9Cr steels, across a range of temperatures, is presented and successfully applied to predict various observed phenomena related to the complex evolution of chemical composition and microstructure.
- The complex microstructure of 9Cr steels, strengthened by dislocations, precipitates, solutes and high- and low-angle grain boundaries, requires a physically-based yield

strength model within component life prediction methodologies to account for microstructure evolution due to interactions of thermal aging, creep, fatigue and oxidation under next generation service conditions.

- A 36% increase in yield strength is observed in cast MarBN compared with rolled P91 steel at 873 K. The proposed new yield strength model predictions show that this increased strength is due to (i) improved solute strengthening via W solute atoms and (ii) a more refined low-angle boundary microstructure, resulting from a finer distribution of $M_{23}C_6$ carbides as tungsten increases.
- The early onset of Fe_2W Laves phase formation with increasing tungsten content is predicted to result in a rapid initial decrease of yield strength under thermal aging conditions. However, once the equilibrium Laves phase volume fraction is achieved, the rate change of yield stress is predicted to reduce significantly. These predictions are consistent with measured observations.
- It is shown that for high (3% wt) tungsten 9Cr steels, significant short-term degradation of yield strength occurs under high temperature conditions due to reduced tungsten-solute strengthening and formation of Fe_2W Laves phase precipitates. In contrast, for lower tungsten ($\leq 1.8\%$ wt.) 9Cr steels, short-term (high temperature) degradation of yield strength is dominated by strain-induced low-angle boundary coarsening and decreased dislocation density.

Acknowledgements

This publication has emanated from research conducted with the financial support of Science Foundation Ireland under Grant Number SFI/14/IA/2604. The authors would also like to acknowledge the contributions made by the collaborators of the MECHANNICS and IMPEL projects, including Mr Rod Vanstone and Mr Bartosz Polomoski of GE Power, Prof Noel O'Dowd of the University of Limerick and Dr David Allen of Impact Power Tech Ltd. In particular, the authors would like to acknowledge Dr Mark Jepson and Mr Juntao Guo of Loughborough University for carrying out ThermoCalc simulations of MarBN and Ms Eimear O'Hara of NUI Galway for the optical micrographs and TEM analysis.

Appendix A: Radii and particle spacing in multi-precipitate type microstructures

For m particle types, the total number of particles per unit volume is defined as:

$$N = \sum_{k=1}^m N_k = \frac{3}{4\pi} \sum_{k=1}^m \frac{f_k}{r_k^3} \quad (\text{A1})$$

where the subscript k denotes each precipitate type in that region, f_k is precipitate volume fraction and r_k is the mean precipitate radius. With reference to the simple geometry of Figure A1, the number of particles per unit volume is inversely proportional to λ^3 , such that the mean spacing of obstacles is defined as:

$$\lambda_i = \left(\frac{4\pi}{3} \right)^{1/3} \left[\sum_{k=1}^m \frac{f_k}{r_k^3} \right]^{-1/3} \quad (\text{A2})$$

where the subscript $i = \text{BND, INT}$ denotes the boundary and LAB interior regions, respectively. The equivalent radius, r_i , for each region is then defined as:

$$r_i = f_i^{1/3} \left[\sum_{k=1}^m \frac{f_k}{r_k^3} \right]^{-1/3} \quad (\text{A3})$$

To enforce the assumption that carbides are dispersed along GBs only in the ‘as received’ microstructure of 9Cr steels, the volume fraction of carbides is modified to the equivalent volume fraction $f_{c,\text{eq}} = f_c / (f_g + f_w)$ [27]. The above approach can also be easily extended to account for Laves phase and Z-phase particles which form in 9Cr steels as a function of thermal aging.

References

1. Morito, S., Yoshida, H., Maki, T., Huang, X. Effect of block size on the strength of lath martensite in low carbon steels. *Materials Science and Engineering A*, **438-440** (2006) 237-240.
2. Sauzay, M., Fournier, B., Mottot, M., Pineau, A., Monnet, I. Cyclic softening of martensitic steels at high temperature - Experiments and physically-based modelling. *Materials Science and Engineering A*, **483-484** (2008) 410-414.
3. Keller, C., Margulies, M.M., Hadjem-Hamouche, Z., Guillot, I. Influence of the temperature on the tensile behaviour of a modified 9Cr-1Mo T91 martensitic steel. *Materials Science and Engineering A*, **527** (2010) 6758-6764.
4. Panait, C.G., Zielińska-Lipiec, A., Koziel, T., Czyska-Filemonowicz, A., Gourgues-Lorenzon, A.-F., Bendick, W. Evolution of dislocation density, size of subgrains and MX-type precipitates in a P91 steel during creep and thermal aging at 600 °C for more than 100,000 h. *Materials Science and Engineering A*, **527** (2010) 4062-4069.
5. Ennis, P.J., Zielinska-Lipiec, A., Wachter, O., Czyska-Filemonowicz, A. Microstructural stability and creep rupture strength of the martensitic steel P92 for advanced power plant. *Acta Materialia*, **45** (1997) 4901-4907.
6. Panait, C.G., Bendick, W., Fuchsmann, A., Gourgues-Lorenzon, A.-F., Besson, J. Study of the microstructure of the Grade 91 steel after more than 100,000 h of creep exposure at 600 °C. *International Journal of Pressure Vessels and Piping*, **87** (2010) 326-335.
7. Srinivas-Prasad, B.S., Rajkumar, V.B., Hari Kumar, K.C. Numerical simulation of precipitate evolution in ferritic-martensitic power plant steels. *CALPHAD: Computer Coupling of Phase Diagrams and Thermochemistry*, **36** (2012) 1-7.
8. Abe, F. Precipitate design for creep strengthening of 9% Cr tempered martensitic steel for ultra-supercritical power plants. *Science and Technology of Advanced Materials*, **9** (2008) 013002.
9. Lacy, C.E., Gensamer, M. The tensile properties of alloyed ferrites. *Transactions of the American Society of Metals*, **32** (1944) 88-110.
10. Abe, F., Tabuchi, M., Semba, H., Igarashi, M., Yoshizawa, M., Komai, N., Fujita, A. Feasibility of MARBN steel for application to thick section boiler components in USC power plant at 650 °C. In: Viswanathan, R., Gandy, D., Coleman, K. (Eds.). *Advances in Materials Technology for Fossil Power Plants. Proceedings from the Fifth International Conference* (2008) p. 92-106.
11. Barrett, R.A., O'Hara, E.M., O'Donoghue, P.E., Leen, S.B. High-temperature low-cycle fatigue behaviour of MarBN at 600 °C. *Transactions of the ASME Journal of Pressure Vessel Technology*, **138** (2016) 021407.
12. Park, J.S., Kim, S.J., Lee, C.S. Effect of W addition on the low cycle fatigue behaviour of high Cr ferritic steels. *Materials Science and Engineering A*, **298** (2001) 127-136.
13. Abe, F., Tabuchi, M., Kondo, M., Tsukamoto, S. Suppression of Type IV fracture and improvement of creep strength of 9Cr steel welded joints by boron addition. *International Journal of Pressure Vessels and Piping*, **84** (2007) 44-52.

14. Magnusson, H., Sandström, R. Influence of aluminium on creep strength of 9-12%Cr steels. *Materials Science and Engineering A*, **527** (2009) 118-125.
15. Peierls, R.E. The size of a dislocation. *Proceedings of the Physical Society*, **52** (1940) 34-37.
16. Nabarro, F.R.N. Dislocations in a simple cubic lattice. *Proceedings of the Physical Society*, **59** (1947) 256-272.
17. Hall, E.O. The deformation and ageing of mild steel: III Discussion of results. *Proc. Phys. Soc. London*, **64** (1951) 747-753.
18. Petch, N.J. The cleavage strength of polycrystals. *J. Iron Steel Inst. London*, **173** (1953) 25-28.
19. Fleischer, R.L. In: Peckner, D. (Ed.). *Strengthening of Metals*. Reinhold: New York, 1964.
20. Labusch, R. A statistical theory for solid solution hardening. *Phys. Stat. Sol.*, **41** (1970) 659-669.
21. Ashby, M.F. In: Gordon and Breach (Eds.). *Proceedings of the Second Bolton Landing Conference on Oxide Dispersion Strengthening*. Science Publishers: New York, 1968.
22. Shibata, A.; Nagoshi, T., Sone, M., Morito, S., Higo, Y. Evaluation of the block boundary and sub-block boundary strengths of ferrous lath martensite using a micro-bending test. *Materials Science and Engineering A*, **527** (2010) 7538-7544.
23. Wang, C., Zhang, C., Yang, Z., Su, J., Weng, Y. Microstructure analysis and yield strength simulation in high Co-Ni secondary hardening steel. *Materials Science and Engineering A*, **669** (2016) 312-317.
24. Li, Q. Modeling the microstructure-mechanical property relationship for a 12Cr-2W-V-Mo-Ni power plant steel. *Materials Science and Engineering A*, **361** (2003), pp. 385-391.
25. Yan, P., Liu, Z., Bao, H., Weng, Y., Liu, W. Effect of microstructural evolution on high-temperature strength of 9Cr-3W-3Co martensitic heat resistant steel under different aging conditions. *Materials Science and Engineering A*, **588** (2013) 22-28.
26. Wang, C., Zhang, C., Yang, Z., Zhao, J. Multiscale simulation of yield strength in reduced-activation ferritic/martensitic steel. *Nuclear Engineering and Technology*, **49** (2017) 569-575.
27. Barrett, R.A., O'Donoghue, P.E., Leen, S.B. A physically-based constitutive model for high temperature microstructural degradation under cyclic deformation. *International Journal of Fatigue*, **100** (2017) 388-406.
28. Kocks, U.F., Argon, A.S., Ashby, M.F. *Progress in Materials Science*, **19** (1975) 156-249.
29. Foreman, A.J., Jawson, M.A., Wood, J.K. Factors controlling dislocation widths. *Proceedings of the Physical Society Section A*, **64** (1951) 156-163.
30. Sakui, S., Sakai, T. The effect of strain rate, temperature and grain size on the lower yield stress and flow stress of polycrystalline pure iron. *Tetsu-to-Hagane*, **58** (1972) 1438-1455.
31. Sakui, S., Sakai, T. The effect of grain size on high temperature plastic deformation of polycrystalline pure iron. *Journal of the Japan Institute of Metals and Materials*, **40** (1976) 263-269.

32. Maruyama, K., Sawada, K., Koike, J.,-I. Strengthening mechanisms of creep resistant tempered martensitic steel. *ISIJ International*, **41** (2001) 641-653.
33. Naylor, J.P. The influence of the lath morphology on the yield stress and transition temperature of martensitic-bainitic steels. *Metallurgical Transactions A*, **10** (1979) 861-873.
34. Varvenne, C., Leyson, G.P.M., Ghazisaeidi, M., Curtin, W.A. Solute strengthening in random alloys. *Acta Materialia*, **124** (2017) 660-683.
35. Zhao, Q., Holmedal, B., Li, Y., Sagvolden, E., Løvvik, O.M. Multi-component solid solution and cluster hardening of Al-Mn-Si alloys. *Materials Science and Engineering A*, **625** (2015) 153-157.
36. Feltham, P. Solid solution hardening of metal crystals. *British Journal of Applied Physics*, **1** (1968) 303-308.
37. Butt, M.Z., Feltham, P. Solid-solution hardening. *Journal of Materials Science*, **28** (1993) 2557-2576.
38. Brandes, E.A., Brook, G.B. *Smithells Metals Reference Book*, 7th Edition. Butterworth-Heinemann: Oxford (1998).
39. Giordana, M.F., Alvarez-Armas, I., Armas, A. Microstructural characterization of EUROFER 97 during low-cycle fatigue. *Journal of Nuclear Materials*, **424** (2012) 247-251.
40. Krauss, G. Martensite in steel: strength and structure. *Materials Science and Engineering A*, **273-275** (1999) 40-57.
41. Mishima, Y., Ochiai, S., Hamao, N., Yodogawa, M., Suzuki, T. Solid solution hardening of nickel - role of transition metal and B-subgroup solutes. *Transactions of the Japan Institutes of Metals*, **27** (1986) 656-664.
42. Miyajima, Y., Ueda, T., Adachi, H., Fujii, T., Onaka, S., Kato, M. Dislocation density of FCC metals processed by ARB. *6th International Conference on Nanomaterials by Severe Plastic Deformation, IOP Conf. Series: Materials Science and Engineering*, **63** (2014) 012138.
43. Reuber, C., Eisenlohr, P., Roters, F., Raabe, D. Dislocation density distribution around an indent in single-crystalline nickel: Comparing nonlocal crystal plasticity finite-element predictions with experiments. *Acta Materialia*, **71** (2014) 333-348.
44. Vicenzo, A. Structure and mechanical properties of electrodeposited nanocrystalline Ni-Fe alloys. *Journal of The Electrochemical Society*, **160** (2013) D570-D577.
45. Thompson, A.W. Effect of grain size on work hardening in nickel. *Acta Metallurgica*, **25** (1977) 83-86.
46. Keller, C., Hug, E. Hall-Petch behaviour of Ni polycrystals with a few grains per thickness. *Materials Letters*, **62** (2008) 1718-1720.
47. Frenzel, J., George, E.P., Dlouhy, A., Somsen, Ch., Wagner, M.F.-X., Eggeler, G. *Acta Materialia*, **58** (2010) 3444-3458.
48. Leyson, G.P.M., Curtin, W.A. Friedel vs Labusch: The strong/weak pinning transition in solute strengthened metals. *Philosophical Magazine*, **93** (2013) 2428-2444.
49. Morito, S., Nishikawa, J., Maki, T. Dislocation density within lath martensite in Fe-C and Fe-Ni alloys. *ISIJ International*, **43** (2003) 1475-1477.

50. Morito, S., Adachi, Y., Ohba, T. Morphology and crystallography of sub-blocks in ultra-low carbon lath martensite steel. *Materials Transactions*, **50** (2009) 1919-1923.
51. Apple, C.A., Caron, R.N., Krauss, G. Packet microstructure in an Fe-0.2% C martensite. *Metallurgical Transactions*, **5** (1974) 593-599.
52. Morito, S., Iwami, Y., Koyano, T., Ohba, T. Effect of solution carbon and nitrogen on the microstructural size and crystallography of lath martensite in Fe-N and Fe-C alloys. *Materials Transactions*, **57** (2016) 227-232.
53. Smith, D.W., Hehemann, R.F. Influence of structural parameters on the yield strength of tempered martensite and lower bainite. *Journal Iron and Steel Institute*, **209** (1971), pp. 476-481.
54. Golden, B.J., University of Limerick, personal communication; 2015.
55. Yan, P., Liu, Z. Toughness evolution of 9Cr-3W-3Co martensitic heat resistant steel during long time aging. *Materials Science and Engineering A*, **650** (2016) 290-294.
56. Jepson, M.A. Loughborough University, personal communication; 2017.
57. Ma, L., Bai, Y., Liu, Z. The Laves phase evolution of 9Cr-3W-3Co steel under long term isothermal treatment. *Steel Research International*, **87** (2016) 1600412.
58. Sha, X., Cohen, R.E. First-principles thermoelasticity of bcc iron under pressure. *Physical Review B*, **74** (2006) 214111.
59. Abe, F. Analysis of creep rates of tempered martensitic 9%Cr steel based on microstructure evolution. *Materials Science and Engineering A*, **510-511** (2009) 64-69.
60. Fedoseeva, A., Dudova, N., Kaibyshev, R. Effect of tungsten on a dispersion of M(C,N) carbonitrides in 9% Cr steels under creep conditions. *Transactions of the Indian Institute for Metals*, **69** (2016) 211-215.
61. Agamennone, R., Blum, W., Gupta, C., Chakravarty, J.K. Evolution of microstructure and deformation resistance in creep of tempered martensitic 9-12%Cr-2%W-5%Co steels. *Acta Materialia*, **54** (2006) 3003-3014.
62. Thomas Paul, V., Vijayanand, V.D., Sudha, C., Saroja, S. Effect of tungsten on long-term microstructural evolution and impression creep behaviour of 9Cr reduced activation ferritic/martensitic steel. *Metallurgical and Materials Transactions A*, **48** (2017) 425-438.
63. Yan, P., Liu, Z., Bao, H., Weng, Y., Liu, W. Effect of tempering temperature on the toughness of 9Cr-3W-3Co martensitic heat resistant steel. *Materials and Design*, **54** (2014) 874-879.
64. Hong, S.G., Lee, W.B., Park, C.G. The effects of tungsten addition on the toughness of modified 9Cr-Mo steels. *Scripta Materialia*, **43** (2000) 181-186.
65. Maddi, L., Barbadikar, D., Sahare, M., Ballal, A.R., Peshwe, D.R., Paretkar, R.K., Laha, K., Mathew, M.D. Microstructure evolution during short term creep of 9Cr-0.5Mo-1.8W steel. *Trans. Indian Inst. Metals*, **68** (2015) S259-S266.
66. Lee, J.S., Ghassemi Armaki, H., Maruyama, K., Muraki, T., Asahi, H. Causes of breakdown in creep strength in 9Cr-1.8W-0.5Mo-VNb steel. *Materials and Engineering A*, **428** (2006) 270-275.
67. Dudova, N., Plotnikova, A., Molodov, D., Belyakov, A., Kaibyshev, R. Structural changes of tempered martensitic 9%Cr-2%W-3%Co steel during creep at 650 °C. *Materials Science and Engineering A*, **534** (2012) 632-639.

68. Li, H., Mitchell, D. Microstructural characterization of P91 steel in the virgin, service exposed and post-service re-normalized conditions. *Steel Research International*, **84** (2013) 1302-1308.
69. Saad, A.A. Cyclic plasticity and creep of power plant materials. Ph.D. Thesis, University of Nottingham, Nottingham, 2012.

Tables

Table 1: Elemental constants for solid solution strengthening [38].

Element	b (nm)	μ (MPa)	ν (-)
Al	0.2863	26.2	0.35
Co	0.2507	82	0.31
Cr	0.2520	115.3	0.21
α -Fe	0.2482	81.6	0.29
γ -Fe	0.2503	81.6	0.29
Mn	0.7718	79.5	0.24
Mo	0.2725	125.6	0.31
Nb	0.2858	37.5	0.4
Ni	0.2492	76	0.31
Si	0.3830	39.7	0.42
Ti	0.2951	45.6	0.32
V	0.2624	46.7	0.37
W	0.2741	160.6	0.28

Table 2: Numerical constants for bcc and fcc phases.

Phase	bcc	Fcc	Source
α_1	0.2	0.5	[39]
M	2.9	3.06	-
α	15	4.4	Fitted
φ	10	11.3	Fitted

Table 3: Chemical composition of low carbon alloys in wt.% [22,49].

Material	C	Mn	Ni	P	S	Si
Fe-1.5Mn	-	1.5	-	-	-	-
Fe-23Ni	<0.01	<0.01	23	0.002	0.003	<0.005
Fe-0.2C	0.18	0.02	-	0.001	0.004	0.006
Fe-0.2C-2Mn	0.206	2.017	-	0.0004	0.0007	0.011

Table 4: Chemical composition of P91 steel, MarBN [8] and G115 [25] steels in wt.%. The balance is made-up of Fe.

	Al	B	C	Co	Cr	Mn	Mo	N	Nb	Ni	P	Si	V	W
P91	0.007	-	0.1	-	8.48	0.42	0.94	0.058	0.073	0.19	0.013	0.26	0.204	-
MarBN (min)	-	0.0047	0.074	2.91	8.77	0.48	-	0.0011	0.046	-	-	0.30	0.18	2.85
MarBN (max)	-	0.018	0.081	3.10	9.08	0.51	-	0.065	0.055	-	-	0.31	0.20	3.13
G115	-	0.013	0.076	2.99	8.83	-	-	0.014	0.042	-	-	-	0.19	3.11

Table 5: Identified microstructural parameters for P91 and MarBN alloys investigated here [7,8,12,32].

Material	d_b (μm)	w (μm)	ρ (m^{-2})	r_{M23C6} (nm)	f_{M23C6} (%)	r_{NbC} (nm)	f_{NbC} (%)	r_{VN} (nm)	f_{VN} (%)
P91	6.7	0.7	1.6×10^{14}	50	2.02	10	0.09	14.5	0.4
MarBN	14	0.325	2.65×10^{14}	83	2.07	7	0.076	20	0.023

Table 6: Microstructural parameters of the 9Cr-Mo-W alloys.

Parameter	9Cr-1Mo	9Cr-0.8Mo-1.2W	9Cr-0.5Mo-1.8W	9Cr-0.1Mo-2.7W
Mo_{eq} (Mo+1/2W)	1	1.4	1.4	1.45
ρ	$1.6 \times 10^{14} \text{ m}^{-2}$	$2.22 \times 10^{14} \text{ m}^{-2}$	$2.56 \times 10^{14} \text{ m}^{-2}$	$2.65 \times 10^{14} \text{ m}^{-2}$
r_{M23C6}	95.0 nm	85.0 nm	83.5 nm	82.5 nm
r_{NbC}	45.1 nm	28.2 nm	26.8 nm	23.9 nm
r_{VN}	16.2 nm	10.6 nm	9.7 nm	10.9 nm
f_{M23C6}	2.09 %	2.27 %	2.36 %	2.49 %
f_{NbC}	0.07 %	0.08 %	0.09 %	0.10 %
f_{VN}	0.21 %	0.25 %	0.28 %	0.31 %
w	0.5 μm	0.418 μm	0.371 μm	0.3 μm
d_b (α')	3.5 μm	3.5 μm	3.5 μm	3.5 μm
d_g (δ -ferrite)	-	-	-	4.5 μm
$f_{\delta\text{-Fe}}$ (δ -ferrite)	-	-	-	8 %

Table 7: Measured evolution of key microstructural parameters under thermal aging in alloy G115 [25,57].

Time	0 hr	300 hr	1000 hr	3000 hr
ρ	$2.65 \times 10^{14} \text{ m}^{-2}$	$2.16 \times 10^{14} \text{ m}^{-2}$	$1.88 \times 10^{14} \text{ m}^{-2}$	$1.87 \times 10^{14} \text{ m}^{-2}$
r_{M23C6}	100 nm	110 nm	120 nm	155 nm
r_{LP}	0 nm	130 nm	145 nm	185 nm
f_{M23C6}	1.13%	1.18%	1.30%	1.29%
f_{LP}	0%	1.72%	2.45%	3.09%
w	0.330 μm	0.350 μm	0.393 μm	0.404 μm
d_g	6 μm	6 μm	6 μm	6 μm

Figures

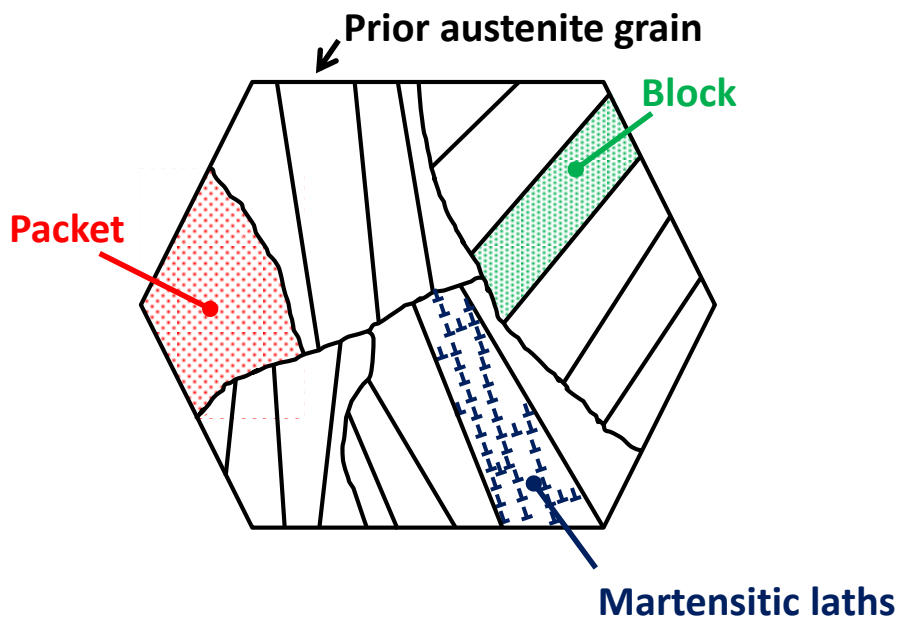


Figure 1: Hierarchical microstructure of 9Cr steels.

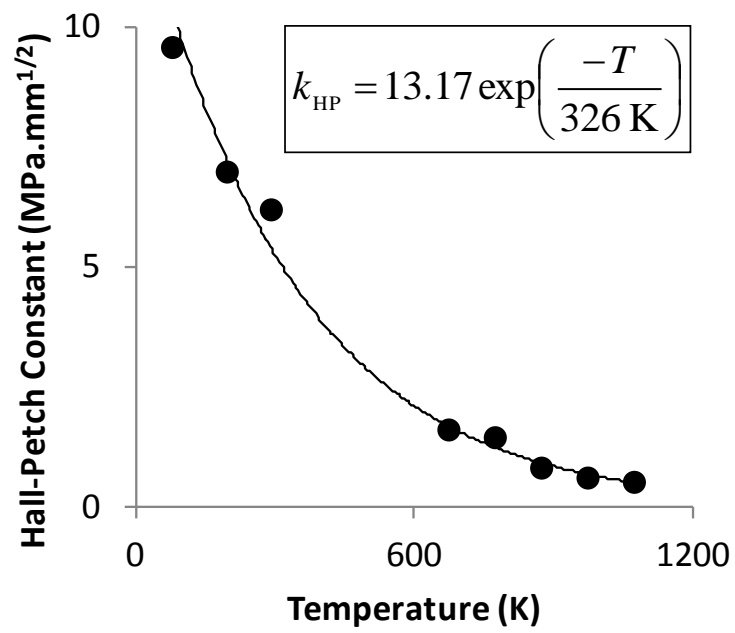


Figure 2: Identified temperature-dependence of the Hall-Petch exponent in pure Fe.

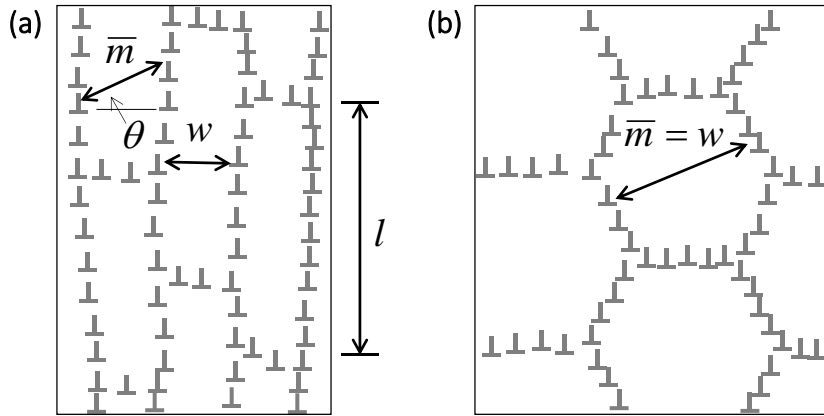


Figure 3: Schematic representation of the mean slip length for (a) martensitic lath and (b) subgrain microstructures.

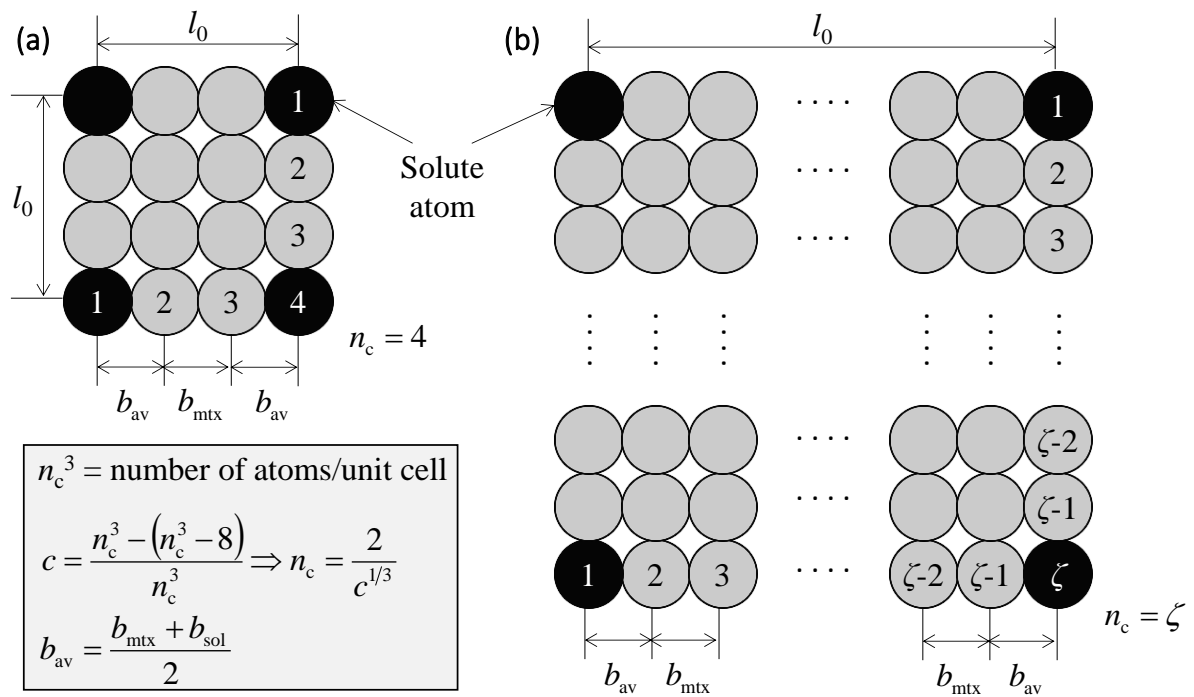


Figure 4: Schematic representation of the determination of the mean solute spacing, l_0 , for (a) a $4 \times 4 \times 4$ atoms unit cell (n_c^3 system, where $n_c = 4$) with $c = 12.5$ at.% and (b) for an infinite system. For simplicity, the model is illustrated for a simple cubic system and is presented in 2D format. Numerical calculations are carried out on a 3D system.

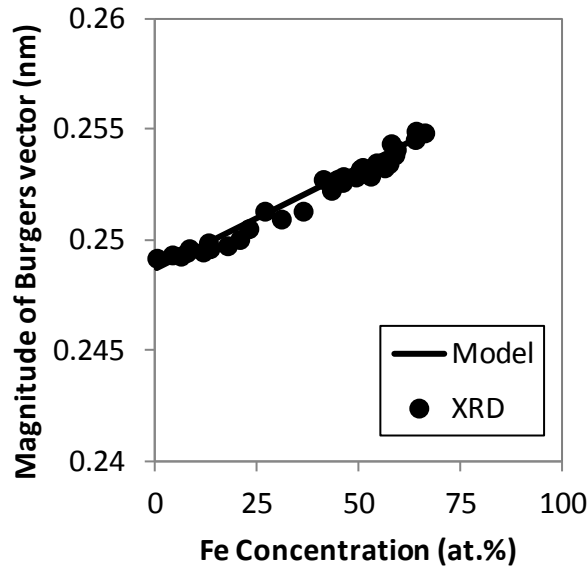


Figure 5: Comparison of the predicted (using a rule of mixtures approach) and measured values of the magnitude of Burgers vector in an fcc Ni-alloy as a function of Fe concentration. The measured values are determined using lattice parameters obtained from the XRD analysis [44].

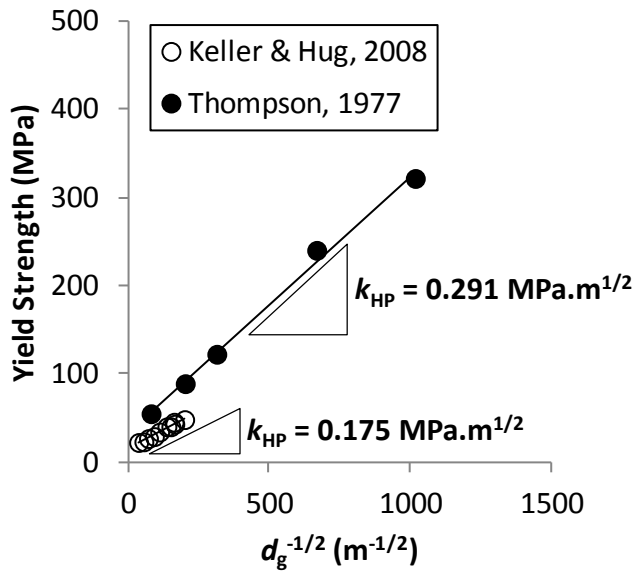


Figure 6: Identification of the Hall-Petch constant for Ni alloy from the measured data of Thompson [45] and Keller and Hug [46].

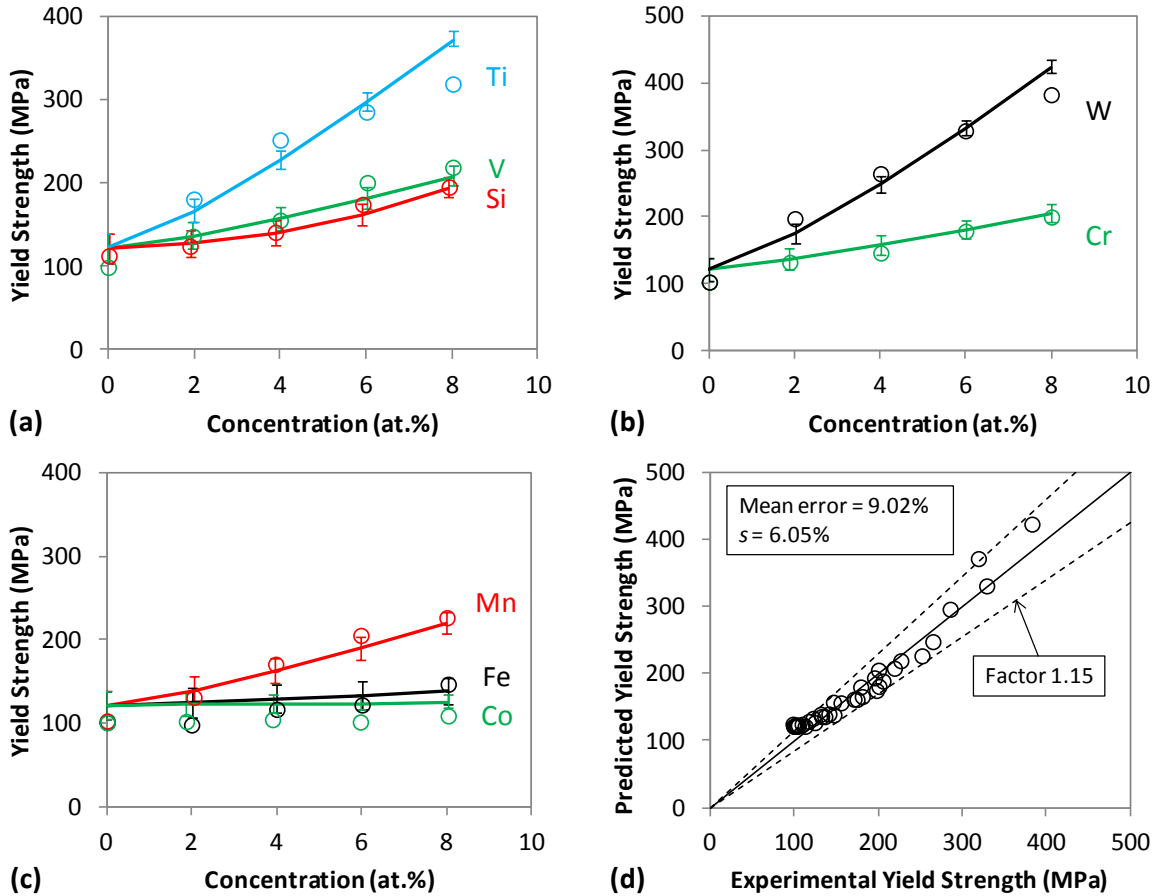


Figure 7: Measured (open symbols) and predicted (solid lines) increase in yield strength associated with the addition of up to 8 at.% substitutional solid solution strengthening in Ni for (a) Group 4, 5 and 14 elements, (b) Group 6 elements, (c) Group 7-9 elements and (d) comparison of the measured and predicted yield strength correlation of all Ni alloys within a factor of 1.15. The measured yield strength data is obtained from [41].

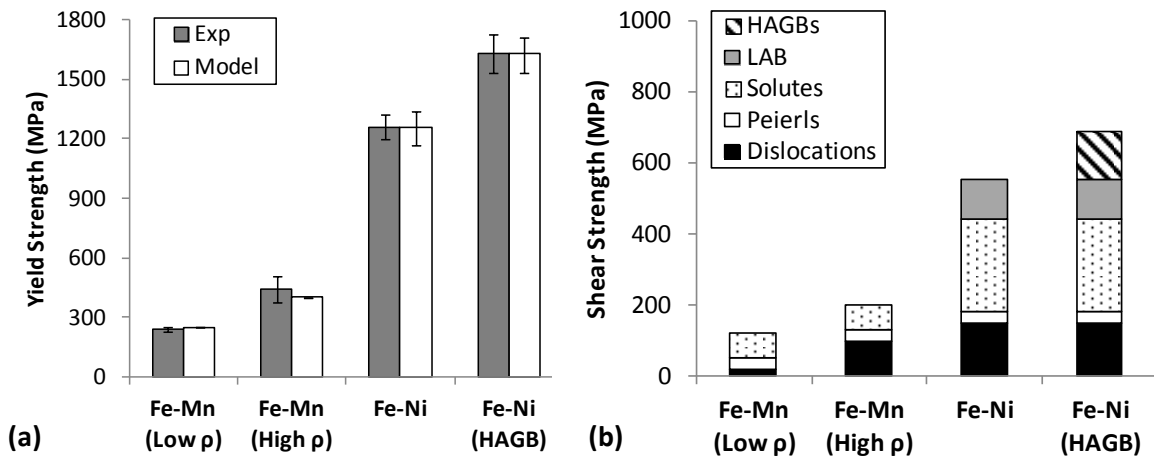


Figure 8: Comparison of (a) predicted and measured yield strength in ferritic (Fe-Mn(Low ρ), Fe-Mn(High ρ)) and martensitic (Fe-Ni, Fe-Ni(HAGB)) alloys and (b) breakdown of the shear stress components contributing to yield strength. The increase in Fe-Mn(High ρ) compared with Fe-Mn(Low ρ) is attributed to the increased dislocation density. The significant increase in yield strength of Fe-23Ni compared with Fe-1.5Mn is attributed to the hierarchical microstructure (LAB and improved dislocation strengthening) and increased substitutional solute strengthening. The effect of HAGB strengthening is successfully predicted via the comparison of yield strength in the martensitic alloy with (Fe-Ni(HAGB)) and without (Fe-Ni) a HAGB.

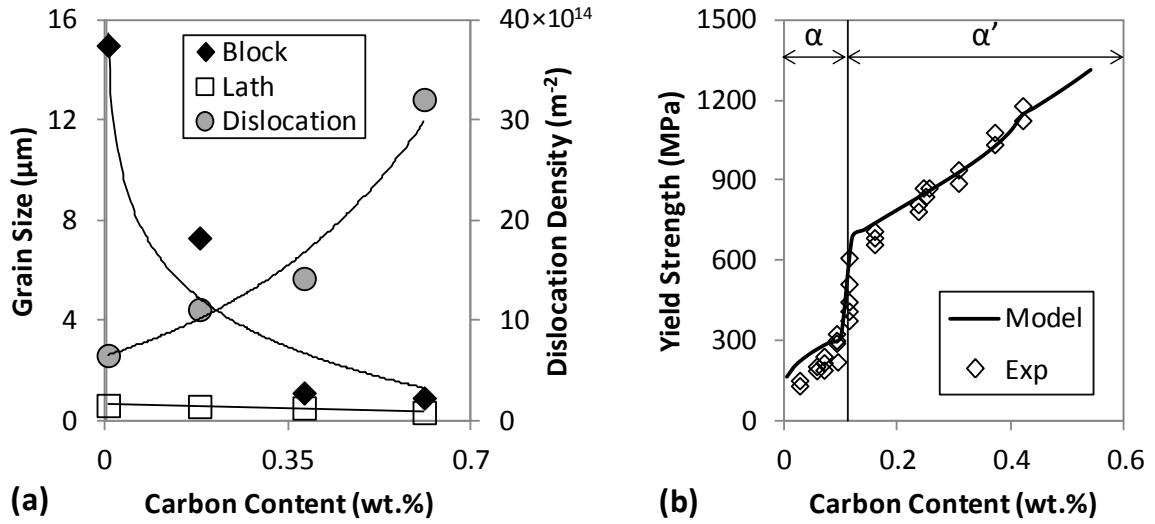


Figure 9: Effect of C content on (a) hierarchical microstructure [49,52] and (b) measured [40] and model predicted yield strength in ferritic (α) and martensitic (α') Fe-C alloys.

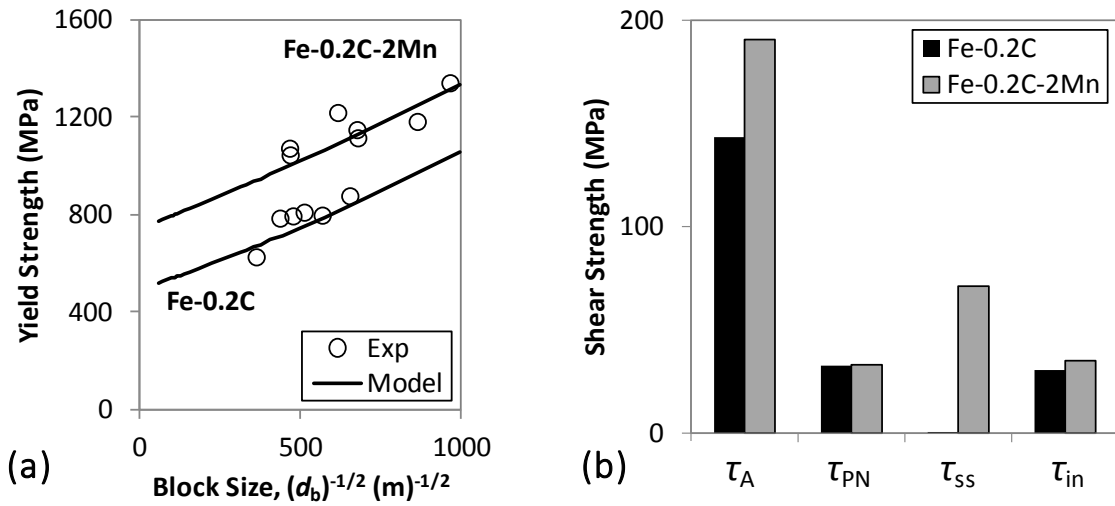


Figure 10: Comparison of the (a) model predicted and experimentally measured yield strength in Fe-0.2C and Fe-0.2C-2Mn alloys as a function of block size and (b) model predicted shear stress contributions. The experimental data is obtained from Morito *et al.* [1].

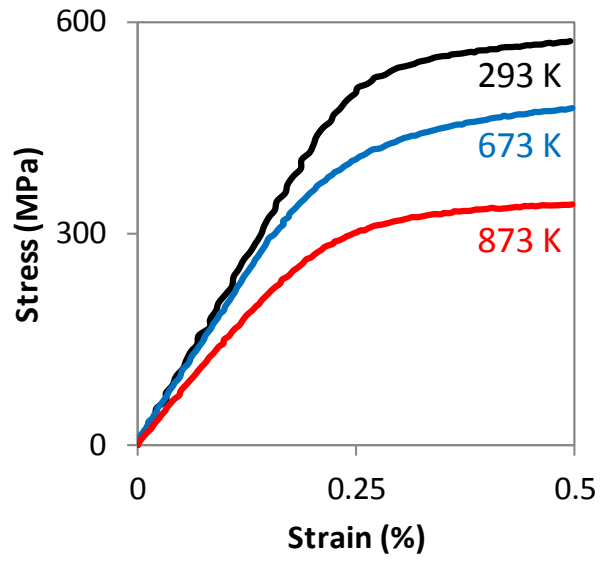


Figure 11: Measured tensile response of P91 steel across a range of temperatures.

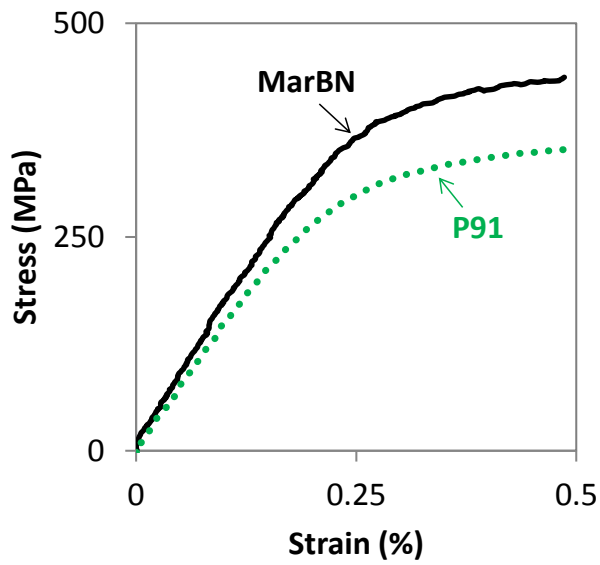


Figure 12: Comparison of the measured tensile response in rolled P91 and cast MarBN at 873 K and applied strain-rate of 0.33 %/s.

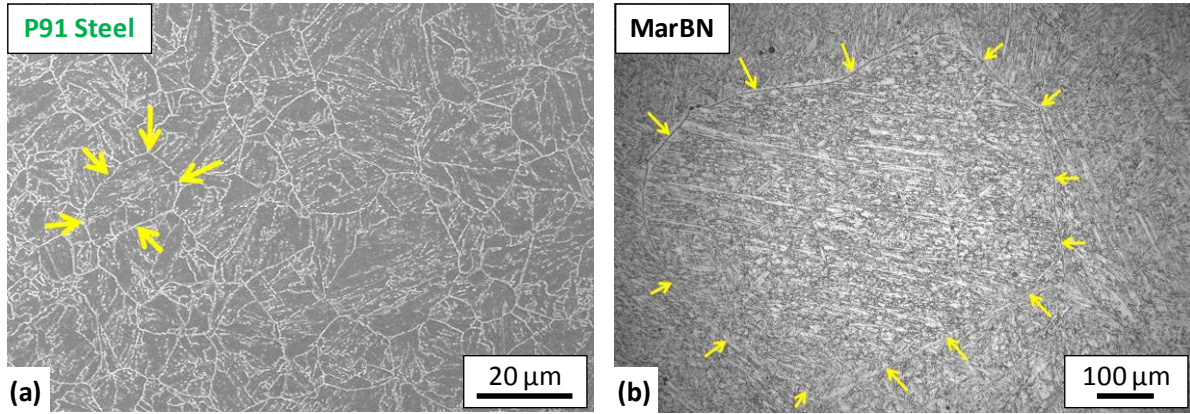


Figure 13: Optical microscope image of the high-angle grain boundary microstructure in (a) rolled P91 and (b) cast MarBN. The arrows demarcate a prior austenite grain boundary.

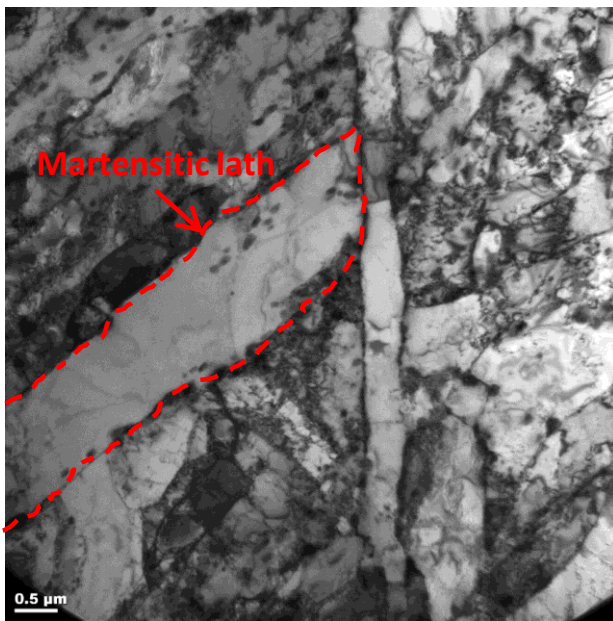


Figure 14: TEM image of the martensitic lath microstructure of cast MarBN.

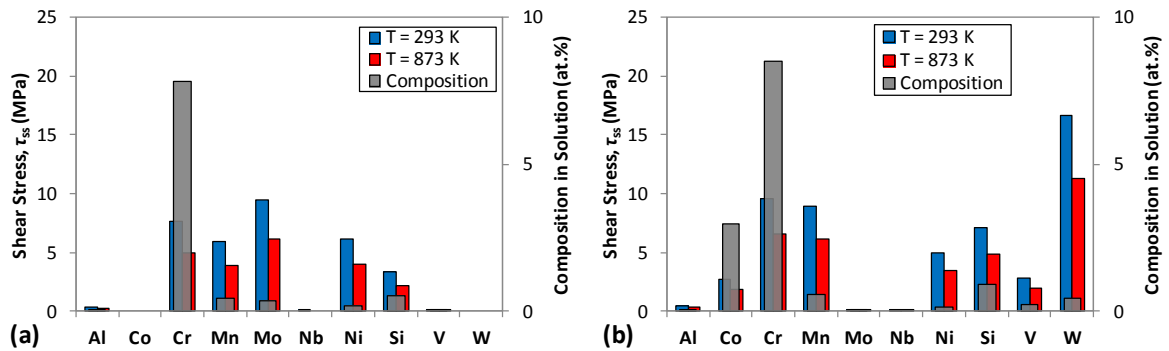


Figure 15: Calculated substitutional solid solution contributions to shear stress at 273 K and 873 K as well as associated composition (at.%) in solution for (a) P91 and (b) MarBN (composition in solution determined using ThermoCalc [56]).

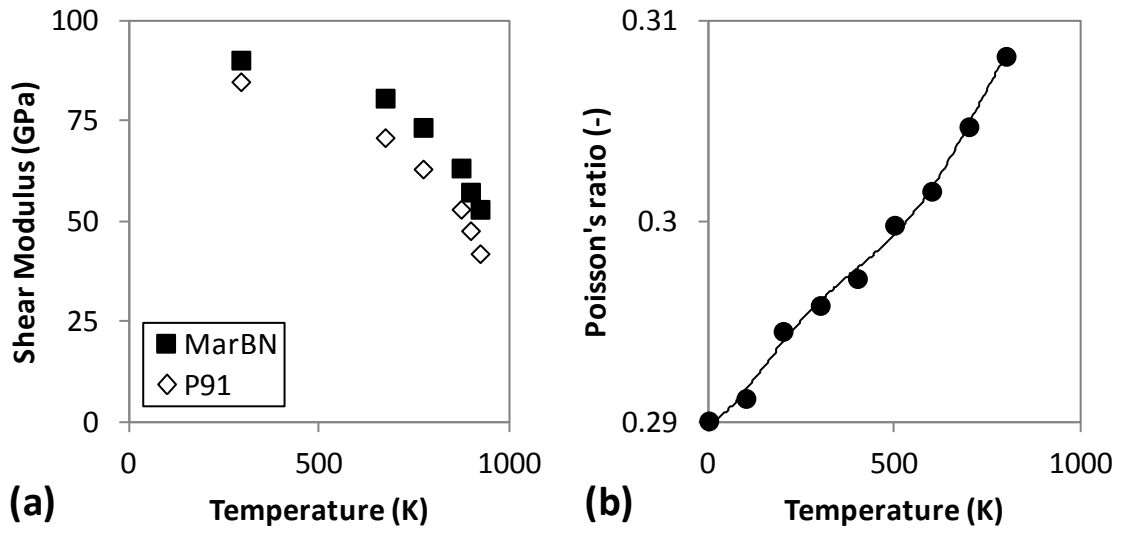


Figure 16: Temperature-dependent (a) shear modulus for P91 and MarBN steels and (b) Poisson's ratio for Fe. The Poisson's ratio is determined based on bulk and shear modulus data of Sha and Cohen [58].

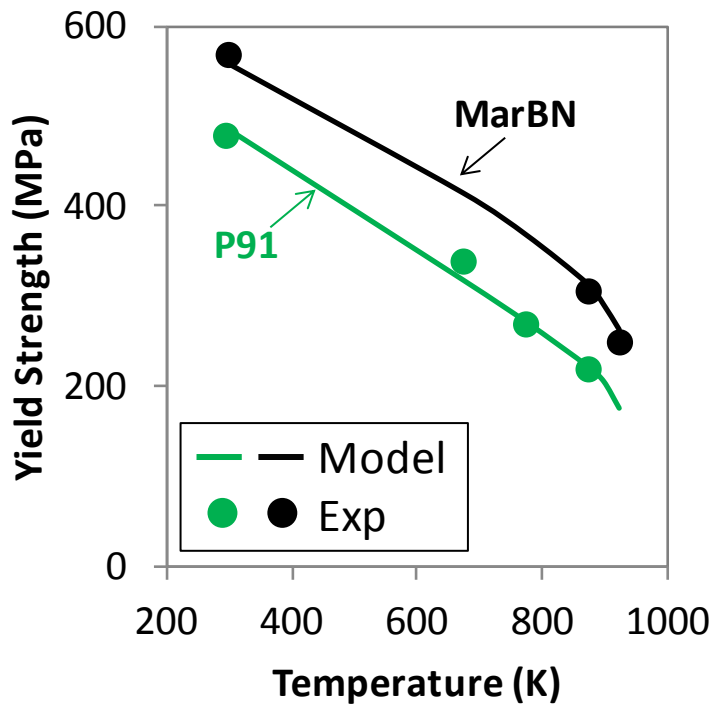


Figure 17: Comparisons of predicted and experimentally measured yield strengths of P91 and cast MarBN alloys as a function of temperature.

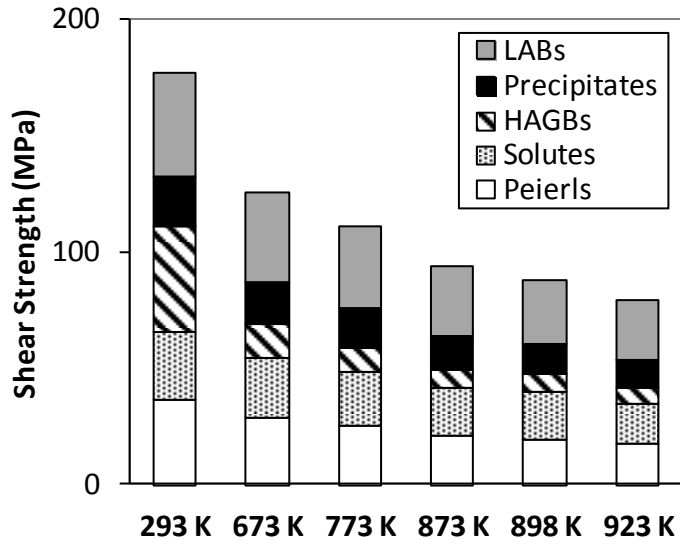


Figure 18: Temperature-dependent shear stress contributions of different obstacles to yield strength in MarBN alloy.

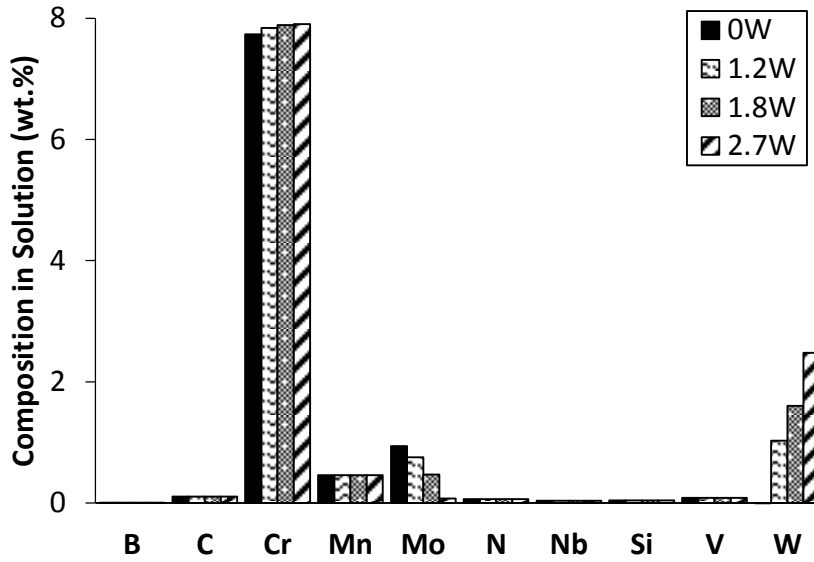


Figure 19: Estimated chemical composition in solid solution form in the 9Cr-Mo-W alloys.

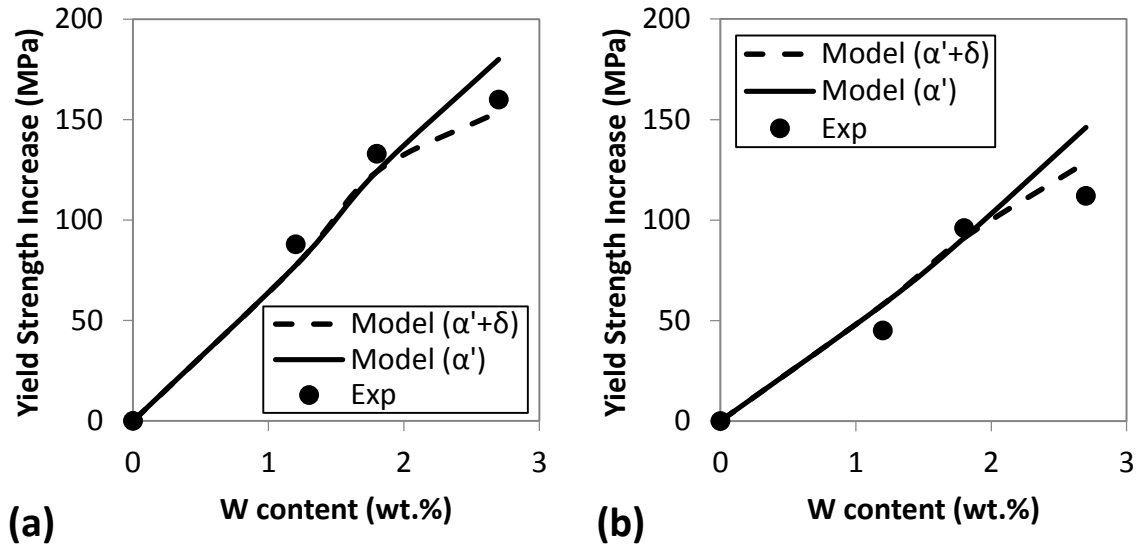


Figure 20: Comparison of the measured [12] and model predicted increase of yield strength as a function of W content at (a) 293 K and (b) 873 K. The dashed line illustrates the yield strength prediction including 8% ferrite for the 2.7W alloy.

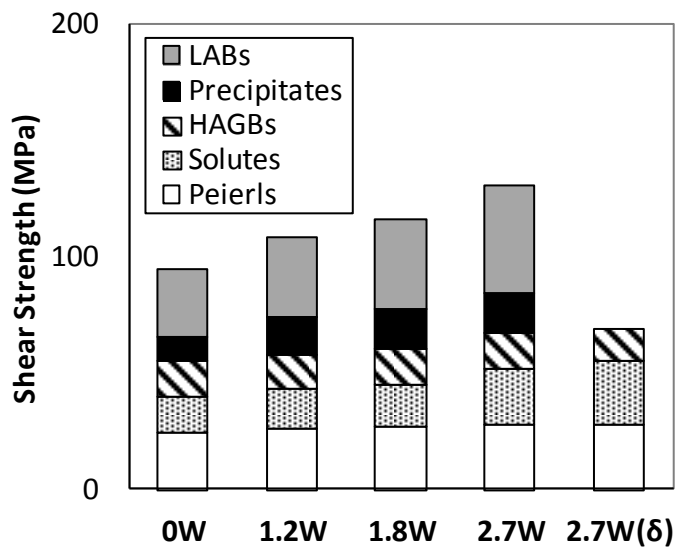


Figure 21: Contributions of the various obstacles to yield strength as a function of W content (wt.%) in Figure 20 at a temperature of 873 K. The '2.7W(δ)' case represents the breakdown of a 100% δ -ferrite alloy with the composition of alloy 2.7W.

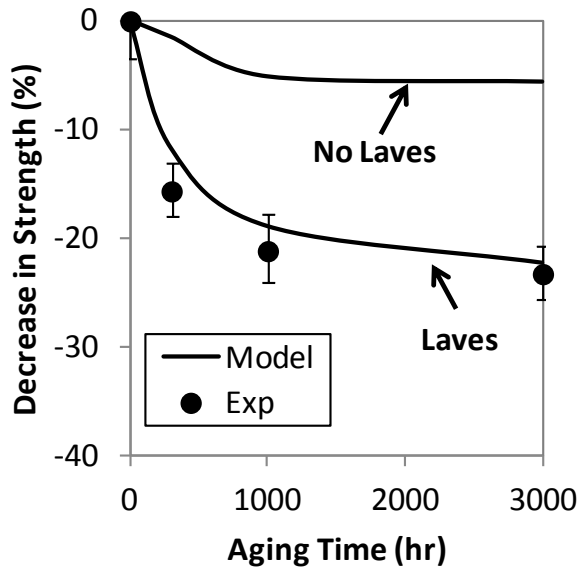


Figure 22: Measured [25] and model predicted decrease of yield strength in a 9Cr-3W-3Co alloy thermally-aged at 923 K. A prediction without the effect of Laves phase (No Laves) formation is also included.

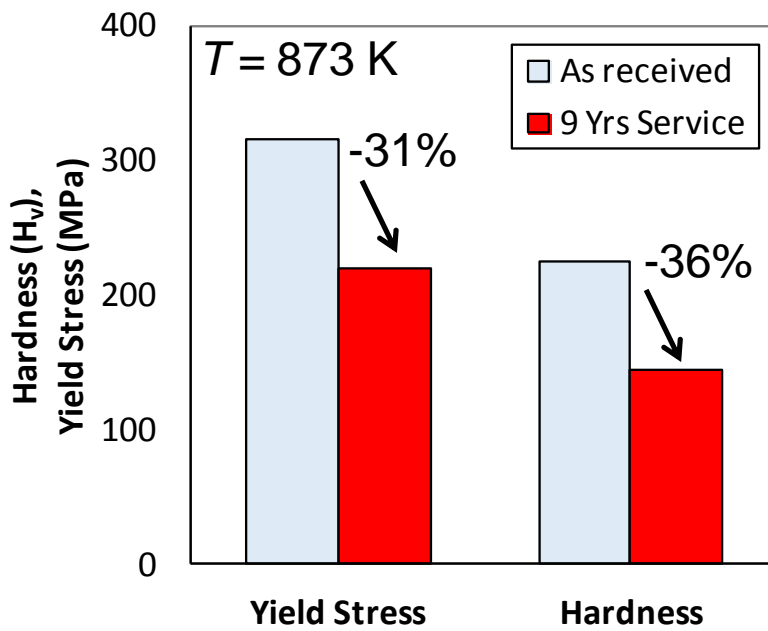


Figure 23: Model predicted yield stress evolution following 100,000 hrs creep deformation and measured [68] 9 year service reduction in hardness of P91 steel at 873 K.

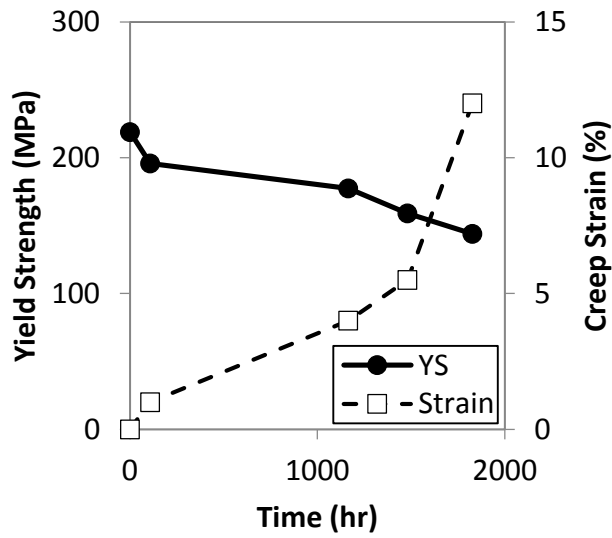


Figure 24: Effect of microstructural evolution on predicted yield strength in a cobalt-modified P92 alloy under creep deformation at 923 K and an applied stress of 140 MPa. The creep strain data is obtained from [67].

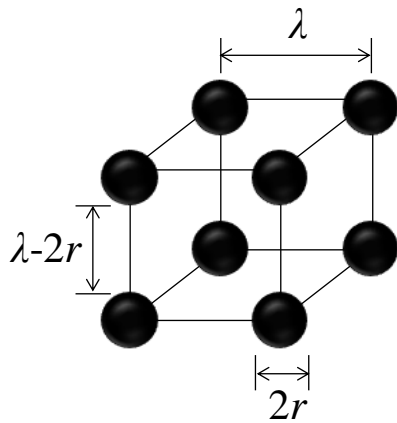


Figure A1: Schematic representation of the precipitate spacing geometric model.